Multi-modal choroid plexus pathology in aging and Alzheimer's disease

Huixin Xu[1] *, Peter Lotfy[2,3,4] *, Benjamin Englert[5 #], Jane Oberhauser[6,7 #], Lillian I.J. Byer[1], Jasmin Wihlman[5,8], Kia Colangelo[5], Serhat V. Okar[9], Ashley Thommana[9,10], Henri Puttonen[5,8], Mikko I. Mäyränpää[5,8], Jarno Tuimala[5], Rute Pedrosa[11], Darshan Kumar[11], James Francis Haberberger[12], Micaiah Emmy Atkins[12], Shon Alimukhamedov[12], Aja Pragana[1], Jordan Benson[1], Mary Elizabeth Gabrielle[1], Anna Dong[1,13], Violeta Durán Laforet[14], Peter Bor-Chian Lin[15], C. Dirk Keene[16], Caitlin S. Latimer[16], Katherine E. Prater[17], David M. Holtzman[15], Alina Isakova[12], Tony Wyss-Coray[12,18], Dorothy P. Schafer[14], Daniel S. Reich[9], Terho Lehtimäki[19,20,21], Pekka J. Karhunen[19,20,21], Eloise H. Kok[19,22], Deidre Jansson[23,24], Andrew C. Yang[6,25,29], Liisa Myllykangas[5,8,29], Jose Ordovas-Montanes[2,4,26,27,28,29], Maria K. Lehtinen[1,3,28,29, †]

*These people contributed equally

#These people contributed equally

Affiliations

[1] Department of Pathology, Boston Children's Hospital and Harvard Medical School, Boston, MA 02115, USA

[2] Division of Gastroenterology, Hepatology, and Nutrition, Boston Children's Hospital, Boston, MA 02115, USA

[3] Graduate Program in Biological and Biomedical Sciences, Harvard Medical School, Boston, MA 02115, USA

[4] Broad Institute of MIT and Harvard, Cambridge, MA 02142, USA

[5] Department of Pathology, University of Helsinki, PO Box 21, 00014 Helsinki, Finland

[6] Gladstone Institute of Neurological Disease, San Francisco, CA 94158, USA

[7] Neuroscience Graduate Program, University of California, San Francisco, San Francisco, CA 94158, USA

[8] HUS Diagnostic Center, Helsinki University Hospital, 00290 Helsinki, Finland

27 [9]Translational Neuroradiology Section, Neuroimmunology Branch, National Institute of
28 Neurological Disorders and Stroke, National Institutes of Health, Bethesda, MD 20815, USA
29 [10] Sidney Kimmel Medical College, Thomas Jefferson University, Philadelphia, PA 19107, USA
30 [11] Aiforia Technologies Plc., 00150 Helsinki, Finland
31 [12] The Phil and Penny Knight Initiative for Brain Resilience, Stanford University, Stanford, CA
32 94305, USA
33 [13] Harvard College, Harvard University, Cambridge, MA 02138, USA
34 [14] Department of Neurobiology, Brudnick Neuropsychiatric Research Institute, University of
35 Massachusetts Chan Medical School, Worcester, MA 01605, USA
36 [15] Department of Neurology, Hope Center for Neurological Disorders, Knight Alzheimer Disease,
37 Research Center, Washington University, St. Louis, MO 63110, USA
38 [16] Department of Laboratory Medicine and Pathology, University of Washington School of
39 Medicine, Seattle, WA, 98057, USA
40 [17] Department of Neurology, University of Washington School of Medicine, Seattle, WA, 98057,
41 USA
42 [18] Department of Neurology and Neurological Sciences, Stanford University, Stanford, CA 94305,
43 USA
44 [19] Faculty of Medicine and Health Technology, Tampere University, 33100 Tampere, Finland
45 [20] Finnish Cardiovascular Research Center, Tampere University, 33014 Tampere, Finland
46 [21] Fimlab Laboratories Ltd., Wellbeing Services County of Pirkanmaa, 33520 Tampere, Finland
47 [22] Tampere University Hospital, Wellbeing Services County of Pirkanmaa, 33520 Tampere,
48 Finland
49 [23] Department of Psychiatry and Behavioral Sciences, University of Washington, Seattle, WA
50 98108, USA
51 [24] VISN 20 Northwest Mental Illness Research, Education and Clinical Center, VA Puget Sound
52 Healthcare System, Seattle, WA, USA

53 [25] Department of Neurology, University of California, San Francisco, San Francisco, CA, USA
54 [26] Program in Immunology, Harvard Medical School, Boston, MA 02115, USA
55 [27] Ragon Institute of MGH, MIT and Harvard, Cambridge, MA 02139, USA
56 [28] Harvard Stem Cell Institute, Cambridge, MA 02138, USA
57 [29] Senior author
58 [†] Correspondence: Maria.Lehtinen@childrens.harvard.edu
59 Co-correspondence: andrew.yang@gladstone.ucsf.edu (A.C.Y.); liisa.myllykangas@helsinki.fi
60 (L.M.); jose.ordovas-montanes@childrens.harvard.edu (J.O-M.);
61 maria.lehtinen@childrens.harvard.edu (M.K.L.)
62

63 **ABSTRACT**

64 Brain barriers, cerebrospinal fluid (CSF) dynamics, and peripheral factors are implicated as
65 significant contributors to Alzheimer's disease (AD). The choroid plexus (ChP) is a blood-brain
66 interface that produces CSF and forms the blood-CSF barrier. However, how ChP pathology
67 develops across the lifespan and contributes to AD has not been systematically characterized.
68 Here, we report a multi-modal ChP atlas integrating single-nucleus transcriptomics from 49
69 individuals, AI-assisted quantitative histopathology across >500 postmortem samples age 16 to
70 105, spatial transcriptomics, and functional studies in 5xFAD mice. We identify fibrosis,
71 calcification, and macrophage abnormalities as hallmarks of ChP aging, with AD pathology
72 conferring additional effects, including expansion of a pro-inflammatory fibroblast-macrophage
73 signaling niche. In 5xFAD mice, macrophage dysfunction is associated with impaired epithelial
74 barrier maintenance and repair. Together, these data provide a foundational resource for
75 understanding ChP dysfunction in aging and AD and propose the macrophage-fibroblast-
76 epithelial barrier axis as a driver of ChP pathology.
77
78

79 **INTRODUCTION**

80 The choroid plexus (ChP) is a secretory epithelial structure in the brain that produces
81 cerebrospinal fluid (CSF) and forms the principal barrier between blood and CSF[1-3]. CSF has
82 been extensively studied as a source of biomarkers for aging and Alzheimer's disease (AD). In
83 AD, changes in CSF amyloid-β and phosphorylated Tau levels predict disease up to 20 years
84 before symptoms appear, and numerous additional biomarkers have since been identified[4-7].
85 Growing evidence also ties peripheral immune cells to brain aging and AD[8,9], including
86 accumulation of inflammatory immune cells in the CSF[10,11]. The ChP both monitors and actively
87 modifies CSF composition through secretion and regulation of immune cell trafficking between
88 the periphery and the central nervous system[12-16]. Therefore, AD-associated changes in CSF hint
89 at possible ChP involvement beginning already from preclinical stages of AD. Clearance of brain
90 waste products, including amyloid-β, through CSF circulation and drainage has emerged as a key
91 contributor to brain homeostasis, and thus, ChP production of sufficient CSF would be cardinal to
92 sustaining CSF flow and brain clearance[17]. However, despite the intimate connection between
93 the ChP and CSF and emerging evidence linking ChP dysfunction to cognitive decline[18-25], the
94 ChP has received far less attention than the blood-brain barrier (BBB), which has been
95 extensively characterized in neurodegeneration[26,27]. Together, these brain barriers protect the
96 central nervous system from peripheral challenges; when compromised, they permit entry of
97 blood-derived factors and immune cells that can facilitate neurodegeneration. While a "leaky" BBB
98 is well established in aging and AD, the status and functional consequences of blood-CSF barrier
99 integrity at the ChP remain incompletely defined.

100 The ChP is located within each brain ventricle and comprises convoluted layers of CSF-
101 facing epithelial cells joined by tight junctions. The underlying stroma consists of fibroblasts,
102 pericytes, and macrophages and is richly vascularized by fenestrated capillaries[1,28]. This
103 architecture supports the dual function of the ChP as both a CSF secretory epithelium and a
104 dynamic barrier between the CSF and blood that selectively gates the entry of blood-borne

105 molecules into the CSF through regulation of tight junctions between epithelial cells[12-14]. This
106 positions the ChP as a hub of body-brain communication whose roles in health and disease are
107 only beginning to be understood. Pathological changes of the ChP are increasingly recognized in
108 aging and neurological diseases[9,29-31], from earlier studies in small cohorts of AD patients showing
109 shortening of epithelial cells and thickening of basement membrane[32], to inflammatory changes
110 in amyotrophic lateral sclerosis[33], fibrosis in multiple sclerosis[34], and formation of Biondi bodies in
111 aging[35,36]. Furthermore, MRI studies consistently report ChP enlargement with age and have
112 identified associations with a number of neurodevelopmental and neurodegenerative disorders[30],
113 including AD. Multiple independent studies have identified an association between ChP
114 enlargement and AD-relevant traits: total ChP volume correlates with cognitive decline,
115 hippocampal shrinkage, and dysfunction of CSF dynamics, while the rate of enlargement is
116 exacerbated by risk factors including female sex and APOE ε4 genotype[19,37-40]. These structural
117 changes are hypothesized to impair ChP function through several proposed mechanisms,
118 including barrier leakage permitting entry of blood-derived factors and immune cells into the CSF,
119 reduced CSF secretion and turnover, and consequently, insufficient clearance of waste and
120 neurotoxic proteins such as amyloid-β.

121 Recent multi-omics studies of human and mouse ChP in AD point towards transcriptional
122 and proteomic changes with implications for ChP epithelial dysfunction and inflammation[41-43].
123 However, the cellular and molecular changes underlying ChP dysfunction across the lifespan
124 have not been systematically defined, precluding identification of specific pathological
125 mechanisms and therapeutic opportunities. Which ChP cell types are affected, what molecular
126 programs drive pathological changes, and whether aging and AD exert separable or synergistic
127 effects remain open questions. Addressing these questions is essential to understanding whether
128 ChP dysfunction represents a cause or consequence of AD and whether it constitutes a tractable
129 therapeutic target.

130 Here, we generated a multi-modal atlas of ChP pathology in aging and AD, integrating
131 studies of human postmortem specimens and mouse models to distinguish age-associated
132 changes from disease-specific effects. We combined single-nucleus RNA-sequencing (snRNA-
133 seq, 49 patients from two cohorts, age range 70-101 years old), 10X Xenium spatial
134 transcriptomics (1 male patient, age 48 years old), Artificial intelligence (AI)-assisted quantitative
135 histopathology (529 patients, age range 16-105 years old), and patient magnetic resonance
136 imaging (MRI) scans (20 patients, age range 31-62 years old). This approach identified extensive
137 fibrosis, calcification, and myeloid cell abnormalities as hallmarks of ChP aging, with sex-
138 dependent effects of AD pathology. We further used a well-established mouse model of amyloid
139 deposition in AD (5xFAD[44]) to dissect ChP changes at early-to-mid stages of AD pathology,
140 independent of aging. Longitudinal *in vivo* two-photon imaging revealed dysregulated
141 macrophage number, morphology, behavior, and recruitment linked to deficits in epithelial barrier
142 maintenance and repair. Together, these data provide a foundational resource for understanding
143 ChP dysfunction and nominate the macrophage-fibroblast-epithelial barrier axis as a candidate
144 driver of ChP pathology in aging and neurodegeneration.
145

146 **RESULTS**

147 **A cellular atlas of the choroid plexus in AD reveals disease-associated inflammatory states**

148 To systematically characterize ChP cellular changes in aging and AD, we generated a
149 snRNA-seq atlas of 197,108 nuclei from postmortem lateral ventricle ChP collected from 49
150 individuals from two independent cohorts: the Religious Orders Study/Memory and Aging Project
151 (ROSMAP; n=31) and the University of Washington Alzheimer's Disease Research Center
152 (ADRC; n=18; **Figure 1A, Supplemental Data 1**). These cohorts included individuals with
153 pathology-confirmed AD (n=21), mild cognitive impairment due to AD (MCI; n=10), and cognitively
154 normal controls without significant neuropathology (n=18) and were balanced for age, sex, APOE
155 genotype, and post-mortem interval (**Figure S1A**). Clinical and neuropathological metadata,

156 including Braak staging and CERAD scores, were not significantly correlated with demographic
157 metrics, including sex, age, or post-mortem interval (**Figure S1B**). Disease and age:disease were
158 shown to be the primary drivers of variance in the dataset, followed by sex and age:sex (**Figure**
159 **S1D**).

160 Following quality control and batch correction with Harmony[45] (**Figure S1C-D**),
161 unsupervised clustering of the integrated dataset identified 14 major cell type clusters. Eight
162 represented canonical ChP-resident and hematopoietic cell types, including endothelial cells,
163 epithelial cells, fibroblasts, pericytes, macrophages, mast cells, T cells, and B cells. The other six,
164 including neurons, astrocytes, ependymal cells, oligodendrocytes, oligodendrocyte precursor
165 cells (OPCs), and microglia, were likely captured during tissue dissection due to the anatomical
166 proximity of the ChP to cortical tissue (**Figure 1B-C**). Gene set enrichment analysis confirmed
167 expected functional profiles: epithelial cells were enriched for ion channel transport, fibroblasts
168 for extracellular matrix (ECM) remodeling, and pericytes for muscle contraction (**Figure S1E**).

169 To define the cellular heterogeneity of the human ChP at higher resolution, we further
170 subclustered these ChP populations hierarchically at two levels (**Figure 1E-G**). First, we
171 subclustered into 21 clusters across all subtypes, revealing further diversity in epithelial cells (2
172 clusters), fibroblasts (4 clusters), and neurons (4 clusters). Epithelial-1 cells were defined by
173 elevated expression of *PDZRN3*, *CDH12*, and *GRM8*, while Epithelial-2 cells were defined by
174 *PLCG2*. Fibroblast-1 cells expressed Complement C3 (*C3*) and *SCUBE1*, Fibroblast-2 expressed
175 contractility genes *MYRIP* and *LAMA2*, Fibroblast-3 expressed the bicarbonate transporter
176 *SLC4A4*, and Fibroblast-4 cells were defined by their expression of *STXBP6* (**Figure 1B-E**).
177 Following exclusion of glial and neural cells, we further subclustered to identify 26 clusters
178 representing transcriptionally distinct cell states (**Figure 1F**). This revealed several clusters of
179 epithelial cells and fibroblasts expressing high levels of inflammatory response genes, including
180 epithelial cells expressing high levels of Oncostatin M receptor (*OSMR*) and its downstream
181 effector *STAT3*, which promotes inflammatory gene expression in response to IL-6 family

182 cytokines. Among fibroblasts, we observed STAT3-high Fibroblasts co-expressing the STAT3
183 target gene *IL4R*[46], interferon-stimulated genes (*MX1*, *ISG15*), and NF-κB-activated fibroblasts
184 expressing *CSF1*, *IL6*, *ICAM1*, and *NFKB1*. The presence of these inflammatory states across
185 multiple ChP cell types suggests coordinated inflammatory signaling within the tissue
186 microenvironment.

187 To determine if these states were enriched in AD, we conducted differential abundance
188 analysis of cell states between AD and control samples. This revealed high enrichment of multiple
189 inflammatory fibroblast states in AD samples, including Cathepsin L (*CTSL*)-positive and IFN-
190 stimulated fibroblasts, though these did not reach statistical significance after multiple hypothesis
191 correction (**Figure 1H**). These trends were instead driven by elevated frequencies in a subset of
192 AD patients rather than a consistent shift across the cohorts, reflecting substantial heterogeneity
193 in fibroblast inflammatory responses among AD individuals. This patient-level variability is
194 consistent with the known clinical and pathological heterogeneity of AD[21] and provides further
195 evidence that fibroblast inflammatory activation may characterize a subset of AD patients rather
196 than a universal disease feature.

197 To infer the upstream signaling pathways driving these transcriptional states, and how
198 they may differ between disease classifications, we conducted ligand activity inference using
199 MultiNicheNet[47] (**Figure 1I**). We observed significant disease-enriched type I and type II interferon
200 (IFN) signaling in fibroblasts and disease-enriched NF-κB signaling in epithelial cells.
201 Furthermore, we found predicted STAT3-related cytokine activity, including Oncostatin M (*OSM*)
202 and IL-20 in the stroma. Together, these findings establish a comprehensive cellular atlas of the
203 human ChP and reveal inflammatory programs that implicate interferon, NF-κB, and STAT3
204 signaling in ChP dysfunction during AD progression.

205

206 **AI-assisted histopathology identifies fibrosis and calcification as age-driven ChP**
207 **pathologies**

208 Given the inflammatory signatures observed in fibroblasts and epithelial cells, we next
209 investigated cellular pathologies using >500 human pathology specimens. We used AI-assisted
210 quantitative histopathology in three independent cohorts of patient specimens to both determine
211 AD pathology-driven versus age-driven changes, focusing on reported hallmarks including
212 fibrosis, psammoma bodies (calcification), and inflammation[30,32]. The first cohort, the Vantaa 85+
213 study, is a population-based cohort consisting of all individuals aged >85 years living in Vantaa,
214 Finland on April 1, 1991[48-50] (n=282; **Supplemental Data 2**). The second cohort, the Tampere
215 Sudden Death Study (TSDS), is a forensic autopsy series comprising white Caucasians[51-53]
216 (n=181; age range 16-90; **Supplemental Data 2**). The third cohort was collected from University
217 of Washington (UW) through Alzheimer's disease research center (ADRC) (n=66; **Supplemental**
218 **Data 2**).

219 Fibrosis and psammoma bodies (calcification) were found to correlate positively with aging
220 in the ChP (**Figure 2A-B**). Masson's trichrome staining was applied to ChP samples to detect
221 connective tissue (collagen) and identify fibrotic ChP villi. We trained an AI model (Aiforia
222 Technologies) to detect ChP tissue area, normal villi, fibrotic villi with increased deposition of
223 connective tissue (**Figure 2A**), and psammoma bodies shown as concentric rings of calcium
224 deposits that accumulated especially within degenerative areas (**Figure 2C**). Fibrosis was
225 calculated by dividing the number of fibrotic villi by the number of normal villi. The number of
226 psammoma bodies was normalized by the tissue area. Both ChP fibrosis and calcification
227 correlated with age. We analyzed fibrosis and psammoma bodies in association with age and
228 various AD pathologies (**Supplemental Data 2**). In the TSDS cohort, fibrosis ($p \leq 0.001$) and
229 psammoma bodies ($p \leq 0.023$) both increased with age. In the Vantaa 85+ cohort, where all
230 subjects were over 85 years old, fibrosis showed a borderline significant association with Thal
231 phases as AD-related pathology ($p \leq 0.054$) and psammoma bodies trended ($p \leq 0.066$) with age in
232 males. In the UW cohort, age- and sex-adjusted analyses showed that psammoma bodies were
233 associated with CERAD ($p \leq 0.022$) and NIA-ABC scores ($p \leq 0.046$). Collectively, our data from

234 multiple independent large cohorts of human samples demonstrated strong age-driven ChP
235 fibrosis and calcification. AD pathology showed moderate association after age-adjusted analyses
236 with some sex-dependence.

237 To validate these findings using orthogonal imaging modalities, we applied Micro-CT
238 imaging of ChP specimens from Vantaa 85+ cohort, confirming age-associated ChP calcification
239 ($p < 0.045$) (**Supplemental Data 2**). Analysis of brain MRI scans from an independent cohort
240 (n=20 multiple sclerosis patients receiving MRIs) revealed that calcification of the lateral ventricle
241 ChP correlated with age but not disease parameters and was notably more extensive in the ChP
242 than in other brain regions. These data suggest that the ChP is particularly vulnerable to age-
243 related calcification (**Figure 2D-F**).

244 To determine the cellular basis of ChP dysfunction and microanatomical heterogeneity in
245 AD, we performed Xenium spatial transcriptomics on the ChP of a 48-year-old, cognitively normal
246 male donor (**Figure S2A-F**), enabling identification of direct cell contacts in the ChP. The spatial
247 data recapitulated all ChP cell types identified in our snRNA-seq dataset and revealed distinct
248 microanatomical localization and spatial niches of different cell subtypes in the ChP stroma,
249 including four subtypes of fibroblasts (**Figure 3A-B**). We found that fibroblasts and macrophages
250 differentially but also preferentially co-localize across ChP spatial niches (**Figure 3B-E, Figure**
251 **S2G)**. Using ligand-receptor interaction analysis in our snRNA-seq dataset, we found that several
252 putative pro-fibrotic and pro-inflammatory fibroblast-macrophage interactions were enriched in AD
253 compared to control, including transforming growth factor β (TGF-β) signaling from macrophages
254 to fibroblasts and collagen-associated factors from fibroblasts to macrophages (**Figure 3F**).
255 Previous work from our group and others has shown that local sources of M-CSF (encoded by
256 *CSF1*) are essential for the maintenance of tissue macrophages[14,54]. We found here that
257 inflammatory fibroblasts are the primary source of CSF1 in the human ChP (**Figure 3G**),
258 suggesting that inflammatory fibroblasts in the ChP promote the retention and recruitment of pro-
259 fibrotic macrophages in AD. Together, these data illustrate that ChP macrophages display a

260 regional, niche-dependent predilection for close physical interaction with ChP fibroblast subtypes
261 and other macrophages or immune cells, suggesting the possibility of a proximity-driven role in
262 later age or disease-related inflammatory processes.

263 Because of this observation and the well-established macrophage-fibroblast circuit[54], we
264 sought out to explore whether a pro-inflammatory fibroblast-macrophage interaction could
265 promote inflammation and ChP dysfunction in aging and AD. To quantitatively analyze
266 macrophage number and inflammation-associated morphological changes, we trained the Aiforia
267 classifier to categorize Iba1+ macrophages by morphology (**Figure 3H**). In Vantaa 85+ cohort,
268 total macrophage coverage ($p \leq 0.003$, **Figure 3I**) and fraction ($p \leq 0.009$) of reactive macrophages
269 associated with age. In men, a positive association between Braak stages (controlled for age)
270 and the fraction of amoeboid macrophages ($p \leq 0.032$), a morphology indicative of a more reactive,
271 pro-inflammatory phenotype, was found. In the UW cohort, an age-association could be seen for
272 the coverage ($p \leq 0.023$) and fraction ($p \leq 0.021$) of rod-shaped macrophages. All other analyses
273 between macrophage morphology and AD pathology or age can be found in **Supplemental Data**
274 **2**. Collectively, our analyses revealed strong age-driven changes in macrophage morphology
275 consistent with increased inflammation. AD pathology showed moderate additional association
276 with some sex-dependence, similar to our observation in fibrosis.

277 While human histopathology revealed robust age- and sex-associated changes in the
278 ChP, the correlation between age and AD pathology in humans limits causal inference. To
279 disentangle these factors and analyze ChP changes in response to a broad range of AD
280 pathologies from mild to severe, we turned to mouse models.

281

282 **Mouse models of AD reveal abnormalities in macrophage behaviors and barrier structure**

283 To isolate AD-associated pathology from normal aging and gain more mechanistic
284 insights, we analyzed the ChP of 5xFAD mice, a mouse model of Aβ amyloidosis, with males and
285 females equally included and analyzed separately, across disease progression (2-9 months of

286 age). Because 5xFAD mice have accelerated AD pathology, we did not detect any fibrosis by 9
287 months of age, which supports the human pathology findings that aging is the main driving force
288 for ChP fibrosis. Instead, we found inflammatory changes occur at early-to-severe-stages of AD-
289 like pathology, some of which appeared prior to extensive plaque deposition. We first
290 characterized ChP macrophages and their responses to early disease pathology. ChP
291 macrophages occupy two distinct anatomical compartments (**Figure S3A**): the apical, CSF-
292 contacting surface of the ChP (epiplexus) and the underlying stromal layers located between
293 epithelial cells and blood vessels (stromal). We previously demonstrated that epiplexus
294 macrophages respond to CSF-derived stimuli, whereas stromal macrophages surveil blood-
295 derived factors[55]. AD pathology alters CSF composition in both human and mouse models,
296 including elevated neurofilament light chain (NfL) and altered Aβ42/40 ratios[4,56,57]. Given their
297 strategic positioning, ChP epiplexus macrophages are well-positioned to sense and respond to
298 these pathological changes. As early as 2 months of age, 5xFAD mice exhibited a striking
299 increase in epiplexus macrophage density compared to wild-type (WT) controls (**Figure 4A-B**),
300 and this elevation persisted at 6 months (**Figure 4C**). At 2 months, 5xFAD mice also showed
301 increased total macrophage coverage (measured by total CX3CR1+ area in wholemount
302 explants) (**Figure 4D**) and longer average process length (**Figure 4E**). By 6 months, total
303 coverage and average process length no longer differed significantly between genotypes;
304 however, 5xFAD mice displayed a subpopulation of epiplexus macrophages with markedly long
305 processes (>75 μm compared to <25 μm typical of WT) as well as a subpopulation of
306 macrophages lacking processes entirely (**Figure 4F**), suggesting increased morphological
307 heterogeneity with disease progression.

308 *In vivo* two-photon imaging revealed distinct macrophage behaviors in 5xFAD mice
309 compared to WT controls. We crossed 5xFAD heterozygous males with *Cx3cr1*^{GFP} reporter
310 females to generate 5xFAD;*Cx3cr1*^{GFP} and WT;*Cx3cr1*^{GFP} littermates for imaging at 6 months of
311 age. Following recovery from cranial window implantation, we administered 70 kDa Texas Red-

312 conjugated dextran intraperitoneally 15 minutes prior to imaging to label blood vessels. Epiplexus
313 and stromal macrophages were distinguished based on their position relative to blood vessels
314 (**Figure 4G**). As illustrated in mice with epithelial cells labeled by *Ttr*^{mNeon}, epiplexus macrophages
315 are visible on top of epithelial cells at a clear distance from blood vessels (**Figure 4G**, outlined),
316 while stromal macrophages lie beneath the epithelium near the blood vessels[14]. Each mouse was
317 recorded across two fields of view for approximately one hour per day over two non-consecutive
318 days. Live imaging revealed several abnormal phenotypes from CX3CR1+ ChP macrophages in
319 5xFAD mice. First, 5xFAD ChP contained focal areas with increased numbers of enlarged
320 epiplexus macrophages (**Figure 4H**, middle; **Supplemental Video V1**) compared to WT controls
321 (**Figure 4H**, left; **Supplemental Video V1**). Second, we observed ameboid epiplexus
322 macrophages containing intracellular dextran reflecting uptake of blood-borne dextran (**Figure**
323 **4H**, right; **Supplemental Video V1**). This intracellular accumulation of dextran may reflect focal
324 epithelial barrier leakage, which was further supported by increased levels of albumin, a blood-
325 derived protein, in the CSF of 5xFAD mice (**Figure 4I**). Consistent with enhanced phagocytic
326 behavior, we also captured epiplexus macrophages containing large cytoplasmic vacuoles
327 resembling those observed in LPS-stimulated cells (**Figure 4J, Figure S3B**). Third, at baseline,
328 epiplexus macrophages are highly mobile with continuously moving cell bodies[55]; however,
329 5xFAD mice harbored epiplexus macrophages with extremely long processes that appeared
330 anchored to the epithelium (**Figure 4K, Supplemental Video V2**). These cells exhibited markedly
331 reduced motility, with their cell bodies showing minimal displacement over 30 minutes compared
332 to the nearly continuous and dynamic repositioning observed in WT controls (**Figure 4K,**
333 **Supplemental Video V2**). These altered morphologies and impaired motility suggest
334 dysregulated macrophage function in 5xFAD mice, potentially associated with compromised
335 barrier integrity.

336 In further support of ChP barrier damage, we observed macrophages clustering near
337 blood vessels in 5xFAD mice. Both whole-mount immunofluorescence and *in vivo* imaging

338 revealed approximately 1-3 distinct macrophage clusters per lateral ventricle ChP in 5xFAD mice,
339 extending from the apical CSF-facing surface through the stroma to the adjacent blood vessels
340 (**Figure 5A-C, Supplemental Video V3**). Strikingly, these clusters were rarely observed in age-
341 matched WT controls. A subset of cells within these clusters expressed high levels of CD45
342 (**Figure 5B**), consistent with recently infiltrated peripheral myeloid cells. The perivascular
343 aggregation of myeloid cells resembles patterns we previously observed in the ChP during laser-
344 induced micro-hemorrhage repair[55], suggesting these clusters may represent sites of vascular
345 damage and active repair.

346 ChP macrophages contribute to maintenance of epithelial tight junctions, which constitute
347 the blood-CSF barrier. In 5xFAD mice, an increased proportion of macrophages contained
348 intracellular Occludin (**Figure 5E**), suggesting enhanced tight junction remodeling. Consistent
349 with barrier disruption, ChP epithelial junctions in 5xFAD mice displayed an irregular, wavy
350 morphology compared to the linear pattern observed in WT controls (**Figure 5F**). We quantified
351 this disruption using a linearity index derived from Occludin immunostaining on whole-mount
352 explants, which revealed significantly disrupted linearity in 5xFAD mice (**Figure 5G**). Electron
353 microscopy combined with intravenous labeling with horse radish peroxidase (HRP) corroborated
354 these immunohistochemical findings (**Figure 5H**).

355 To test whether 5xFAD mice exhibit impaired barrier repair capacity, we challenged mice
356 with intracerebroventricular (ICV) lipopolysaccharide (LPS). We previously demonstrated that ICV
357 LPS causes severe disruption of tight junction proteins (including Occludin, Claudin-2, and ZO-
358 1), with partial recovery by 5 days post-challenge[14]. As expected, both WT and 5xFAD mice
359 displayed comparably disrupted tight junctions 24 hours following LPS while 5xFAD mice showed
360 baseline damage consistent with what we observed before (**Figure S4**). However, 5xFAD females
361 showed significantly delayed barrier recovery at 7 days post-challenge, assessed by Claudin-2
362 expression patterns and tight junction linearity index (**Figure 5J**). These findings indicate that

363 amyloid-β pathology impairs the capacity of the ChP to restore barrier integrity following
364 inflammatory challenge, especially in females.

365 ChP epithelial cells are long-lived[1] and thus may be particularly vulnerable to accumulating
366 senescence-associated damage. Given that recent work has shown that cellular senescence in
367 the ChP drives age-dependent barrier dysfunction through irregular remodeling of tight junction
368 proteins by senescent macrophages[58], we asked whether amyloid-β pathology accelerates ChP
369 cellular aging, We analyzed the ChP from *in situ* transcriptomics data generated from 9-month-
370 old 5xFAD and WT mouse brains. Using a consensus senescence-associated gene signature[59-
371 61], we found that several ChP cell types in 5xFAD mice, including epithelial, mesenchymal, and
372 immune cells, exhibited elevated senescence scores compared to WT controls (**Figure 5K-L**).
373 These findings suggest that amyloid-β pathology promotes premature cellular aging in the ChP,
374 which may contribute to our observations of dysregulated macrophage behaviors and barrier
375 dysfunction in 5xFAD mice.

376

377 **Sexually dimorphic myeloid cell recruitment to the ChP in mouse AD models**

378 Peripheral immune cell recruitment often accompanies barrier disruption. At 2 months of
379 age, 5xFAD mice had increased numbers of ameboid CD45-high cells compared to WT controls
380 (**Figure 6A-B**), consistent with increased peripheral cell infiltration. However, by 6 months, the
381 difference was no longer significant (**Figure 6C**), paralleling the contrast we observed with
382 macrophage coverage and process lengths (**Figure 4D-E**). These data suggest that peripheral
383 immune cell infiltration is most pronounced during early pathology, at the onset of Aβ plaques in
384 this model.

385 Single-cell RNA-sequencing of the ChP from 6-month-old 5xFAD and WT mice revealed
386 sex-biased transcriptional responses following the initial wave of immune cell infiltration (**Figure**
387 **S5, Supplemental Data 3**). Female 5xFAD macrophages specifically upregulated chemokines
388 that recruit CCR2+ monocytes (e.g., *Ccl2*, *Ccl7*, and *Ccl12*) compared to female WT and male

389 5xFAD macrophages (**Figure 6D**). We also observed sex-dependent changes in the resident ChP
390 macrophage pool. Using the *Ccr2*^{GFP} reporter line to distinguish between recently recruited
391 immune cells and ChP-resident macrophages, we classified GFP+ cells as ameboid (infiltrated
392 monocytes) or ramified (newly differentiated macrophages). Female 5xFAD mice exhibited
393 significantly increased numbers of GFP+ ramified cells compared to female WT controls (**Figure**
394 **6E-F**), indicating enhanced monocyte-to-macrophage differentiation. The difference was not
395 observed in male mice due to high variations both at in WT and in 5xFAD mice. Using two-photon
396 *in vivo* imaging, we captured a small number of CCR2+ cells within each FOV. CCR2+ cells in
397 5xFAD females spanned a greater distance than those in WT controls (**Figure 6G-H,**
398 **Supplemental Video V4**).

399 To determine whether female-biased macrophage recruitment generalizes to other AD-
400 relevant pathologies, we examined the P301S transgenic tau mouse model of tauopathy with a
401 knock-in of humanized *APOE* ε3 or ε4 alleles at 9 months of age[62,63]. Consistent with our 5xFAD
402 findings, we observed increased numbers of newly derived CD45-high macrophages in female,
403 but not male, P301S mice compared to WT controls (**Figure 6I-K**). Male mice had higher level of
404 CD45-high macrophages at baseline and did not show further recruitment in response to
405 pathology. This macrophage recruitment was independent of human *APOE* allele status. Notably,
406 P301S mice did not exhibit the increase in total or epiplexus macrophage numbers observed in
407 5xFAD mice, suggesting that epiplexus macrophage expansion may be specific to Aβ pathology,
408 whereas enhanced monocyte recruitment and macrophage turnover at the ChP may represent a
409 broader feature of AD-associated ChP inflammation.

410

411 **DISCUSSION**

412 The ChP is the principal source of CSF and a critical barrier regulating molecular and
413 cellular trafficking between the periphery and CNS, relaying inflammatory information between
414 the brain and the periphery in both directions[14,22]. Despite mechanistic work demonstrating that

415 inflammation in the ChP negatively impacts animal cognition[25], clinical studies that increasingly
416 link larger ChP volume to cognitive decline[37-39,64], and CSF proteomics identifying ChP dysfunction
417 as a distinct molecular subtype of AD[21], the contribution of ChP pathology to aging and AD has
418 not been systematically characterized. Here, we present a multi-modal atlas that was generated
419 by integrating snRNA-seq, spatial profiling, AI-assisted quantitative histopathology, patient MRIs,
420 and *in vivo* two-photon imaging paired with transcriptomics and mechanistic studies in mouse
421 models to define the cellular and molecular landscape of ChP dysfunction in aging and AD.

422 Our work underscores the importance of a holistic and integrative approach to understand
423 ChP pathology. Characterization of both human and mouse ChP at the transcriptional level
424 provided valuable knowledge in understanding this brain barrier. Early work identified age-driven
425 reduction in the expression of ion transporters and tight junction proteins by quantitative-PCR,
426 hinting at reduced CSF production and barrier damage. ScRNAseq and snRNA-seq datasets, as
427 well as epigenomics, from human tissues and animal models further revealed the molecular and
428 cellular architecture of the ChP and its responses towards different brain conditions, such as
429 healthy aging[28], COVID infection[22], and AD[42,43]. More recently, our *in vivo* imaging findings
430 emphasize the importance of going beyond transcriptomics[14]. For example, we observed a
431 diverse set of abnormal behaviors by ChP macrophages of 5xFAD mice (**Figures 4-6**), revealing
432 complexity of ChP macrophage responses towards AD pathology that was not captured by
433 transcriptomics. Therefore, a holistic approach that integrates unbiased transcriptomics datasets
434 with studies of cell functions is essential to fully understand how the ChP functions in health and
435 diseases.

436 A central finding of our study is that aging alone drives substantial ChP fibrosis,
437 calcification, and macrophage dysfunction, whereas AD pathology exerts moderate additional
438 effects with notable sex-differences. The broad age range of the TSDS study enabled us to
439 establish that ChP structural changes emerge independent of dementia status, consistent with
440 lifespan imaging studies showing ChP aging signatures appearing around age 30[65] and

441 transcriptomic shifts occurring later at 50-60 years old[66]. Furthermore, MRI studies demonstrate
442 age-related increases in ChP volume are accompanied by reduced blood perfusion at the
443 ChP[67,68]. This temporal framework wherein ChP pathology precedes the onset of clinical AD
444 suggests that age-related barrier dysfunction may render the brain vulnerable to subsequent
445 neurodegenerative insults. Altogether, our data support a model in which age-related ChP
446 deterioration precedes and may facilitate AD progression. If so, interventions targeting ChP aging
447 may represent a strategy to delay or prevent the development of AD, especially in high-risk
448 populations. Distinguishing cellular changes driven by AD pathology versus normal aging is a
449 major challenge for mechanistic studies of AD. Recent work suggest that the brain may take up
450 two distinct trajectories of cellular changes, leading to either AD or alternative aging[69]. Further
451 analyses of ChP fibrosis and calcification in patients with other age-related neurodegenerative
452 disorders or in patients with familial AD or Down Syndrome who are at high risk of developing AD
453 at relatively younger ages, may bring deeper understanding of the contribution of age-driven ChP
454 fibrosis to neurodegeneration.

455 The stromal fibrosis and calcification we identified likely have significant functional
456 consequences. Recent studies of meningeal lymphatics found that age-related ECM remodeling
457 impedes CSF clearance[70]. Likewise, the increased fibrosis and calcification of the ChP stroma
458 could block water movement from fenestrated capillaries to epithelial cells. Compounded by other
459 age-associated changes in ChP epithelial cells including stunting of microvilli[71], formation of
460 Biondi bodies[35,36], and downregulation of CSF secretory machinery (e.g., NKCC1[28,72]), the
461 additional fibrotic changes in the ChP stroma may contribute to the well-established reduction of
462 CSF secretion with advanced age[73], and thereby allow amyloid-β buildup and the onset of
463 Alzheimer's disease. It is of further interest to understand the timeframe of the onset of different
464 ChP pathologies and whether, in addition to cell autonomous changes, fibrosis and calcification
465 could promote epithelial pathology by altering blood-to-epithelial cell trafficking.

466 Fibroblasts have emerged as key contributors to fibrosis and calcification following injury
467 and disease in the central nervous system[74,75], with recent studies showing that fibroblasts rapidly
468 give rise to profibrotic myofibroblasts following CNS injury[75,76]. Critically, this response involves
469 bidirectional crosstalk where macrophages promote myofibroblast activation through TGF-β,
470 while activated fibroblasts reciprocally support macrophages through M-CSF, which is encoded
471 by *CSF1*[75]. Moreover, fibroblast-mediated collagen deposition disrupts lymphatic drainage and
472 CSF clearance[70], which could negatively impact removal of Aβ or inflammatory cytokines in the
473 milieu. Our snRNA-seq data revealed that inflammatory fibroblast subsets were enriched in AD
474 (**Figure 1H**) and exhibited elevated expression of extracellular matrix factors (**Figure 3F**) as well
475 as upregulated *CSF1* signaling **(Figure 3G).** Spatial transcriptomics demonstrated that fibroblasts
476 and macrophages occupy overlapping stromal niches within the human ChP (**Figure 3A-E**), and
477 cell-cell interaction analyses identified crosstalk between macrophages and inflammatory
478 fibroblasts mediated by *CSF1* and TGF-β (**Figure 3F**), in line with mouse studies of CNS
479 injury[75,76]. A concurrent multi-omics study of the ChP in the ROSMAP cohort similarly identified
480 ECM pathway dysregulation in fibroblasts, but noted only mild collagen accumulation in AD, a
481 discrepancy we attribute to the depth of our AI-assisted quantitative histopathology, which
482 captured the strong age- and sex-driven effects on the development of ChP fibrosis[42]. Future
483 studies may explore whether therapeutic targeting of fibroblast-macrophage interactions could
484 limit the development of fibrosis and calcification in the ChP to preserve barrier function during
485 brain aging, as suggested by studies in other brain compartments[77].

486 Our mouse studies provide mechanistic insight into how macrophages contribute to barrier
487 dysfunction during early AD-like pathology. *In vivo* two-photon live imaging of 5xFAD mice
488 revealed that abnormal macrophage phenotypes, including increased phagocytic uptake of blood-
489 sourced dextran, perivascular clustering, and reduced motility occurred prior to extensive plaque
490 deposition and were accompanied by increased tight junction uptake in macrophages, irregular
491 tight junction morphology, and delayed barrier repair upon inflammatory challenge. These findings

492 extend previous work showing that ChP macrophages coordinate barrier disruption and repair
493 through direct remodeling of epithelial tight junctions in acute inflammation[14] and aging-associated
494 senescence[58]. Analysis of spatial transcriptomics data from 5xFAD mice revealed elevated
495 senescence signatures in ChP epithelial cells and macrophages, suggesting that amyloid
496 pathology may promote premature senescence-associated dysfunctions in barrier maintenance
497 (**Figure 5K-L**). Furthermore, barrier compromise can enable pathological immune cell entry into
498 the CSF and brain parenchyma, where their abundance negatively correlates with cognition[10,11].
499 Our observation that infiltration of CD45-high cells during early-stage AD-like pathology suggests
500 that macrophage-mediated barrier dysregulation may facilitate such infiltration. Future work
501 should determine whether the molecular underpinnings of ChP macrophage dysfunction extend
502 their influences beyond the blood-CSF barrier to affect brain-wide inflammation.

503 Sex differences in AD prevalence remain incompletely understood. MRI studies show that
504 females exhibit a more than two-fold greater rate of ChP enlargement compared to males[38], while
505 mouse studies have shown female-biased hippocampal microglial senescence and inflammation
506 during aging that may contribute to sex differences in AD prevalence[78]. We observed sex-
507 dependent changes in both patient samples and mouse models. In human samples, we found
508 that males had a stronger association between ChP fibrosis and calcification and AD pathology.
509 In mouse models, we observed enhanced macrophage recruitment in the females of both the
510 5xFAD model for amyloid pathology and the P301S model for tauopathy. Our scRNA-seq of
511 5xFAD mice supported the histological observation by showing female-specific upregulation of
512 macrophage-secreted CCR2 ligands. Recent work also reported sex differences in ChP
513 macrophages and secretome, with immune signatures enriched in females[79]. Collectively, these
514 data raise questions about whether males and females may have different mechanisms
515 underlying ChP damage or repair, which then contribute to differences in AD risk and progression,
516 warranting further investigation.

517 Our atlas highlights the value of combining postmortem human studies and early
518 pathology investigations with animal models. However, our findings also reveal the limitations in
519 the current models to study the ChP in aging and AD, shown primarily by the failure of mouse
520 models to recapitulate pro-fibrotic transcriptomic signatures and pathology. Commonly used AD
521 mouse models do not capture the complex genetic backgrounds of human patients. These
522 models, especially 5xFAD mice, also have accelerated pathology and do not model age-driven
523 changes like fibrosis. Other humanized models such as iPSC, microfluid 3D models, and
524 organoids reflect the genetic complexity of humans and have demonstrated their potential in
525 bridging human pathology studies and functional investigation *in vitro*[80-83], but it remains
526 challenging to retain cellular aging features as the process fosters rejuvenation. Likewise,
527 common mouse models like 5xFAD mice have accelerated pathology, meaning the animals do
528 not incorporate age-driven changes, such as fibrosis. New advances in human stem cell
529 technology and humanized mouse models combining multiple known genetic contributors will
530 provide more physiologically relevant AD models in the future.
531

532 **Limitations of the study**

533 Our analysis on human pathology has several limitations: the TSDS cohort's wide age
534 range enabled identification of age-associated pathology, but the lack of detailed medical history
535 makes it challenging to analyze AD associations compared to studies using other conventional
536 AD-oriented brain banks. Second, the Vantaa85+ cohorts represent a more restricted age range
537 (>85 years of age), and thus also limits our ability to disentangle disease phenotypes from age.
538 Lastly, while we aim to delineate age contribution versus AD disease contribution to ChP
539 pathology, in most patients, age and AD pathology are not independent. While our data
540 demonstrate strong age-associated pathological changes in the ChP such as fibrosis,
541 calcification, and macrophage types, the lack of a strong association with AD pathology after
542 normalizing for age should not be interpreted as evidence that AD pathology has a weak impact

543 on the ChP. In contrast, our studies in mouse models support a strong impact of AD pathology on
544 ChP cell functions. In addition, our pathology specimens were restricted to portions of the lateral
545 ventricle ChP. How ChP in the third and fourth ventricles change with aging and AD remains
546 undetermined, and whether fibrosis and calcification demonstrate spatial specificity within each
547 ChP is unknown. Future human studies with broader age ranges, more spatial coverage of ChP
548 from different brain ventricles, and thorough disease diagnosis, including longitudinal imaging
549 studies, will provide further understanding on ChP dysregulation in response to AD pathology.
550

551 **ACKNOWLEDGEMENTS**

552 We thank members of the Lehtinen, Ordovas-Montanes, Myllykangas, Wyss-Coray, and Yang
553 labs for helpful discussions, Andreea Luchian for her support with Aiforia methodology, Onerva
554 Levälampi, Kristiina Nokelainen, Nina Hankonen for excellent technical assistance, the Boston
555 Children's Hospital Cell Discovery Network for advice on computational analysis, and Nancy
556 Chamberlin for critical reading and editing of the manuscript. We thank the following facilities and
557 personnel: Chinfei Chen, Hisashi Umemori, Cheng-Hao Chien, Harry Cramer, and the BCH
558 IDDRC Cellular Imaging Core; Harvard Medical School Electron Microscopy Facility; FIMM Digital
559 Microscopy and Molecular Pathology Unit supported by HiLIFE and Biocenter Finland for slide
560 scanning services; and The Sanderson Center for Optical Experimentation at University of
561 Massachusetts Chan Medical School. We thank the Vantaa 85+ Study establishers, researchers,
562 and collaborators over the years as well as the participants, their families, and carers. We thank
563 the personnel of Tampere University Histology Facility 'Histocore'. We thank Lisa Keene, Emily
564 Ragaglia, Aimee Schantz, and Kathryn Torrez, for incredible administrative support, John
565 Campos and Mark Montine for data management, and Angela Wilson, Amanda Keene, Jenna
566 Kelley, Julia Ryan, Flavia Ernau, Kim Howard, and Katie Miller for outstanding technical
567 support. We are deeply grateful to the research participants and their families without whom this
568 work would be impossible.

This work was supported by: BrightFocus postdoctoral fellowship in Alzheimer's Disease research A2022026F and Boston Children's OFD/BTREC/CTREC Faculty Career Development Award (H.X.); Howard Hughes Medical Institute James H. Gilliam Fellowship for Advanced Study (P.L.). The National Multiple Sclerosis Society (Postdoctoral Fellowship Grant, FG-2208-40289) (S.V.O.). Abramson Fund for Undergraduate Research, Stone Father-Daughter Fund for Undergraduate Research, and Herchel Smith Undergraduate Science Research Fellow (A.D.). BrightFocus Foundation A2022006F (V.D.L.), Alzheimer's Association AARF-22-923219 (V.D.L.). ADRC Development Award (UW, P30AG066509 D.J.). The UW BioRepository and Integrated Neuropathology (BRaIN) Laboratory and Precision Neuropathology Core are supported by the National Institutes of Health (NIH) through the UW Alzheimer's Disease Research Center (P30AG066509), the Adult Changes in Thought (ACT) study (U19AG066567 and R01AG060942), the BRAIN Initiative Cell Atlas Network (UM1 MH130981 and UM1MH134812), the Seattle Alzheimer's Disease Brain Cell Atlas (U19AG060909), cooperative agreements (U24AG072458; U24NS133949; U24NS133945; U24NS135651; U01NS137500; and U01NS137484), the US Department of Defense (DoD W81XWH-21-S-TBIPH2), the Chan-Zuckerberg Initiative, and the Allen Institute for Brain Science. Dr. Keene is additionally supported as a Weill Neurohub Investigator and the Nancy and Buster Alvord Endowed Chair in Neuropathology. AHA–Allen Initiative in Brain Health and Cognitive Impairment (19PABHI34580007) (T.W.-C and A.C.Y.), the Michael J. Fox Foundation (T.W.-C.), The Phil and Penny Knight Initiative for Brain Resilience (T.W.-C. and A.I.). NIMH-R01MH113743 (D.P.S.), NINDS-R01NS117533 (D.P.S.), NIA-R01AG068281 (D.P.S.), Cure Alzheimer's Fund (D.P.S.), the Miriam and Sheldon G. Adelson Medical Research Foundation (D.P.S.). U19AG069701 (D.M.H.), NS090934 (D.M.H.), and the Freedom Together Foundation (D.M.H.). This research was supported in part by the Intramural Research Program of the NIH (D.S.R.). The contributions of the NIH authors are considered Works of the United States Government. Cure Alzheimer's

595 Fund (D.S.R.); Adelson Family Foundation (D.S.R.); Jane and Aatos Erkko Foundation (P.J.K.);
596 Finnish Foundation for Cardiovascular Research (P.J.K. and T.L.); Finnish Cultural Foundation
597 (E.H.K.). National Institute of Neurological Disorders and Stroke 1R01NS128909-01 and
598 1RF1NS139975-01 (A.C.Y.). Academy of Finland (341007, L.M.), HUS Diagnostic Center and
599 Helsinki University Hospital competitive research fund (TYH2022316, L.M.) Liv och Hälsa
600 foundation (L.M.), Finska Läkaresällskapet (L.M) and Jane and Aatos Erkko Foundation (L.M.).
601 The Pew Charitable Trusts Biomedical Scholars, The Broad Next Generation Award, NIH R01
602 HL162642, and The Cell Discovery Network at Boston Children's Hospital supported by the
603 Manton Foundation and Warren Alpert Foundation (J.O.-M.); The New York Stem Cell Foundation
604 – Robertson Investigator (J.O.-M.); Cure Alzheimer's Fund (M.K.L., and L.M.), Sigrid Jusélius
605 Foundation (M.K.L.), and NIH R01 NS088566, NS129823, RF1048790 (M.K.L.); BCH IDDRC
606 1U54HD090255 and NIH grant #S10OD030322. The findings and conclusions presented in this
607 paper are those of the authors and do not necessarily reflect the views of the NIH or the U.S.
608 Department of Health and Human Services.

609

610 **DISCLOSURE**

611 D.S.R. has received research funding from Abata and Sanofi. D.M.H. co-founded and is on the
612 scientific advisory board of C2N Diagnostics. D.M.H. is on the scientific advisory boards of Denali,
613 Genentech, Cajal Neuroscience, and Switch and consults for Pfizer, Novartis, and Roche. D.M.H.
614 is on the advisory board of *Neuron* and *Cell*. J.O.-M. reports compensation for consulting services
615 with Tessel Biosciences, Radera Biotherapeutics, and Passkey Therapeutics.

616

617 **AUTHOR CONTRIBUTIONS**

618 H.X., P.L., D.J., A.C.Y., L.M., J.O.-M., and M.K.L. conceptualized and designed the study; H.X.,
619 P.L., B.E., J.O., J.W., R.P., D.K., S.V.O., V.D.L., D.J., D.P.S., E.H.K., D.S.R., A.C.Y., L.M., J.O.-
620 M., and M.K.L. established methodology; H.X., P.L., B.E., L.I.J.B., J.W., K.C., H.P., A.P., J.B.,

621 M.E.G., V.D.L., E.H.K., A.C.Y., S.A., M.E.A, and D.J. conducted experiments; H.X., P.L., B.E.,
622 J.O., J.W., K.C., H.P.,M.I.M., J.T., J.F.H., S.A., S.V.O., A.T., A.D., K.E.P., J.F.H., V.D.L., D.S.R.,
623 A.C.Y., L.M., J.O.-M., and M.K.L. analyzed data; P.L. C.D.K., C.S.L., D.M.H., D.P.S., D.S.R.,
624 T.W.-C., A.I., P.J.K., T.L., and E.H.K. provided experimental material; D.J., D.S.R., T.W.-C., A.I.,
625 D.P.S., P.J.K., A.C.Y., L.M., J.O.-M., M.K.L. provided funding and supervised the study; H.X.,
626 P.L., B.E., J.O., J.W., L.M., J.O.-M., and M.K.L. wrote the manuscript. All co-authors read, revised,
627 and approved the manuscript.
628

629 **METHODS**

630 **Data and Code Availability**

631 1. Human snRNA-seq data and mouse scRNA-seq data will be made publicly accessible on
632 synapse.org (project number syn71304114) upon publication. The datasets are available
633 for visualization through Broad Institute single cell portal under project ID SCP3449
634 (human) and SCP3451 (mouse).
635 2. Raw sequencing reads for mouse scRNA-seq data will be available in GEO upon
636 publication. All other original data are available from the Dr. Lehtinen upon request. All
637 biological materials were either directly commercially available or are available upon
638 request.
639 3. All MATLAB code used in this study are published[55] and available on Github at
640 https://github.com/LehtinenLab/Shipley2020.
641 4. Availability of other source data and any additional information required to reanalyze the
642 data reported in this paper are available from the lead contact upon request.
643

644 **EXPERIMENTAL MODEL AND SUBJECT DETAILS**

645 **Human Subjects**

646 Single-nucleus RNA-sequencing cohorts

647 Two independent cohorts of frozen lateral ventricle ChP were used. The first cohort was
648 obtained from Rush University's Religious Orders Study/Memory and Aging Project and the
649 second was collected by the Neuropathology Core of the Alzheimer's Disease Research Center
650 (ADRC) of the University of Washington (UW) at autopsy. Tissue was flash frozen and stored at
651 -80C. All samples were collected with approval from local ethics committees and in accordance
652 with institutional review board guidelines. Complete neuropathological examination for all tissue
653 samples was carried out as previously described.

654 Histopathology cohorts:

655 1. The Vantaa 85+ study, a population-based cohort of the oldest old, consists of individuals aged
656 >85 years living in Vantaa, Finland on April 1st, 1991 (n=601, n=282 analyzed). Their key
657 demographic and neuropathologic variables are shown in **Supplemental Data 2**. Exact
658 descriptions of the cohort have been published previously. Each participant and/or their relatives
659 gave informed consent for the study. The collection of tissue samples and their research use was
660 approved by the Finnish national authority of medicolegal affairs. The ethical committees of the
661 Helsinki University Hospital and the City of Vantaa approved the study.

662 2. The Tampere Sudden Death Study (TSDS) is comprised of 515 white Caucasian men and 185
663 white Caucasian women aged 16–97 years subjected to a medicolegal autopsy at the Department
664 of Forensic Medicine, University of Tampere, Finland, between 2010 and 2015. The TSDS series
665 covered approximately 20% of deaths in the region during the timeframe of the study collection.
666 According to Finnish legislation, the indications for a medicolegal autopsy include sudden
667 unexpected out-of-hospital death, accident, suspected suicide, or homicide. In Finland, individual
668 informed consent is not required from autopsy cases or their next of kin in a forensic study setting.
669 The Ethics Committee of Pirkanmaa Hospital District (Permission numbers R09097 and R16199)
670 and the National Supervisory Authority for Welfare and Health (Valvira Document number
671 564/05.01.00.06/2010) approved the TSDS protocol. Previous descriptions of the cohort have
672 been reported[51-53]. A subset of cases (n=181) with a sufficient portion of ChP tissue attached to

673 the hippocampus section were analyzed in this study. Key demographic and neuropathological
674 variables are shown in **Supplemental Data 2**.
675 3. University of Washington cohort. As described above, choroid plexus tissue from the lateral
676 ventricles was collected by the Neuropathology Core of the Alzheimer's Disease Research Center
677 (ADRC) of the University of Washington (UW) at autopsy (**Supplemental Data 2**). Paraffin
678 embedded tissue blocks were sectioned, processed, and analyzed at University of Helsinki.
679 Spatial transcriptomics
680 Postmortem human brain tissue was obtained from the Lieber Institute (Johns Hopkins
681 University) and processed by the Knight Initiative for Brain Resilience (Stanford University), with
682 approval from local ethics committees.
683 Patient MRI
684 Clinical and imaging data was collected from participants with multiple sclerosis (MS)
685 (including radiologically isolated syndrome, RIS)[84] or MS-mimicking diseases under the
686 institutional review board-approved National Institute of Neurological Disorders and Stroke
687 protocol, "Evaluation of Progression in Multiple Sclerosis by Magnetic Resonance Imaging"
688 (NCT00001248). Written, informed consent was acquired from participants. Participants were
689 categorized as having relapsing MS (RMS) or progressive MS (PMS)[85]. Participants who did not
690 meet diagnostic criteria for MS4 or RIS and demonstrated neuroinflammatory symptoms with
691 abnormal MRI were categorized as other inflammatory neurological disease (OIND). Age at scan
692 time, disease modifying therapy (DMT) status, Expanded Disability Status Scale (EDSS)[86],
693 Scripps Neurological Rating Scale (SNRS)[87], Symbol Digit Modalities Test (SDMT)[88], and Paced
694 Auditory Serial Addition Test (PASAT)[89] scores were recorded when available.
695
696 **Animal studies**
697 The Boston Children's Hospital IACUC and University of Massachusetts, Amherst
698 approved all experiments involving mice in this study. The following genetic strains were obtained

699 from JAX laboratory: C57BL/6J (000664), 5xFAD (034848), *Cx3cr1*^{GFP} (005582), *Ccr2*^{GFP}
700 (027619), *Cx3cr1*^{CreER} (020940), Ai14 (007914). 5xFAD mice (B6.Cg-
701 Tg(APPSwFlLon,PSEN1*M146L*L286V)6799Vas/Mmjax, RRID:MMRRC_034848-JAX) was
702 obtained from the Mutant Mouse Resource and Research Center (MMRRC) at The Jackson
703 Laboratory, an NIH-funded strain repository, and was donated to the MMRRC by Robert Vassar,
704 Ph.D., Northwestern University. All 5xFAD mice used in this study were bred by crossing 5xFAD
705 male with C57BL/6J female, and the offsprings were housed separately by both genotype and
706 sex. P301S mice were bred in the Holtzman lab and crossed with humanized APOE3 or
707 APOE4[62,63]. Both male and female mice were equally included in the study. TTRmNeon mice
708 were generated at Boston Children's Hospital and published previously[14,90]. Animals were housed
709 in a temperature-controlled room on a 12-hr light/12-hr dark cycle and had free access to food
710 and water.
711

712 **METHOD DETAILS**

713 **Isolation of nuclei from human choroid plexus tissue**

714 ROSMAP cohort: Nuclei isolation was performed as previously described[22]. Briefly, 40 mg of
715 choroid plexus tissue was thawed in 250 µl of 1% BSA with 0.2 U µl−1 RNase inhibitor. The tissue
716 was incubated in 5 ml of lysis buffer (10 mM Tris, 10 mM NaCl, 3 mM MgCl2, 0.1% Nonidet P40
717 substitute (Roche/Sigma, 11754599001), 0.2 U µl−1 RNase inhibitor, and protease inhibitor) on
718 ice for 10 min with gentle swirling every 2 min. 5 ml of 1% BSA was added and the tissue triturated
719 10 times with a 5-ml serological pipette. After centrifugation (500g, 5 min), pelleted nuclei were
720 resuspended in 1% BSA with 0.2 U µl−1 RNase inhibitor, gently triturated 10 times with a 1-ml
721 regular-bore pipette tip and filtered twice through a 70-µm and then a 40-µm strainer (Flowmi).
722 Debris was inspected on a brightfield microscope and nuclei were counted on an TC20 automated
723 cell counter (Bio-Rad) after the addition of Trypan blue.

724 University of Washington cohort: Frozen choroid plexus tissue (80-100 mg) was sampled on dry
725 ice and mechanically minced with scalpels in sterile Petri dish on ice. Tissue dissociation method
726 was adapted from a previous protocol[91] with modifications. Tissue was transferred to 1.5 ml
727 microcentrifuge tube (Fisherbrand ™ Pellet Pestle™ Microtubes 12-141-365) containing 250 µl
728 TST buffer (Table 1-2). Tissue was manually homogenized with pestle (Fisherbrand™ RNase-
729 Free Disposable Pellet Pestles, Cat. No. 12-141-364), pestle rinsed with 500 µl TST. Tissue was
730 rotated at 4 °C for 10 minutes, and filtered through 40 µm filter (Corning, Cat. No. 352340).
731 Samples were centrifuged at 500 *x* g, 4 °C for 5 minutes, and pellet was resuspended in 1 ml ST
732 buffer with RNase inhibitor (Table 1) and DAPI staining solution (1/1000, Abcam, Cat. No.
733 ab228549) for 10 minutes. Nuclei were isolated on the SONY cell sorter SH800S with a 100 µm
734 chip and collected in nuclei suspension buffer (Table 3).

735

736 Table 1: 2X ST buffer

Chemical	**Company**	**Cat. No.**
292 mM NaCl	Thermo Fisher Scientific	AM9759
20 mM Tris-HCl pH 7.5	Thermo Fisher Scientific	15567027
2 mM $CaCl_2$	VWR International Ltd	97062-820
42 mM $MgCl_2$	Sigma Aldrich	M1028

737

738 Table 2: TST buffer

Chemical	**Company**	**Cat. No.**
1 ml 2X ST buffer		
60 µl of 1% Tween-20	Sigma-Aldrich	P-7949
10 µl of 2% bovine serum albumin (BSA)	Sigma-Aldrich	A3294
920 µl of nuclease-free water	Fisher Scientific	10-977-023

10 μl (5 μl/mL) Protector RNase Inhibitor (2000 units)	Sigma-Aldrich	3335399001

739

740 Table 3: Nuclei suspension buffer

Chemical	**Company**	**Cat. No.**
500 μl 10% bovine serum albumin (BSA)	Sigma-Aldrich	A3294
500 μl 1mM Aurintricarboxylic acid (ATA) in PBS	Sigma-Aldrich	A1895
4 ml 1X PBS	Fisher Scientific	AM9625
(5 μl/ml) Protector RNase Inhibitor	Sigma-Aldrich	3335399001

741 *filtered prior to addition of RNase inhibitor

742 **Single-cell dissociation of mouse choroid plexus**

743 The lateral ventricle (LV) ChP was dissected in cold RPMI media with 10mM HEPES and
744 minced with a pair of fine scissors in a 1.5 ml tube (approximately 200 times until only small pieces
745 remained). LV ChP from 3 adult male mice were pooled into each sample. Tissue pellets were
746 digested in an enzyme cocktail containing collagenase P (0.5 mg/ml, Sigma cat. 11213865001),
747 dispase (0.8 mg/ml, Worthington cat. LS02104), and DNAse1 (250 U/ml, Worthington cat.
748 LK003172) for 30 min. at 37° C with slow head-to-toe rotation. Post-digestion tissues were
749 washed, triturated, and filtered with 70 μm mesh. All pipette tips and tubes were coated by
750 incubating in HBSS containing 2% BSA. For scRNA-seq preparation, to avoid transcriptional
751 changes during the dissociation process, dissection and digestion solutions contained
752 actinomycin (Sigma, cat. A1410, 5 μg/ml), triptolide (Sigma, cat. T3652, 10 μM), and Anisomycin
753 (Sigma, cat. A9789, 27.1 μg/ml) [92]. For CSF analysis, CSF from 5 adult male mice were collected
754 and pooled into each sample. The CSF was treated with ACK lysing buffer (Thermo Fisher
755 A1049201) to remove red blood cells. Cells from CSF were pelleted at 1000 g x 10 min. (4° C)
756 and washed.

757

758 **Droplet-based sequencing**

759 Human snRNA-seq: Libraries were prepared using the Chromium Next GEM Single Cell 3' v.3.1
760 according to the manufacturer's protocol (10x Genomics), targeting 10,000 nuclei per sample. For
761 the ROSMAP cohort, 15 cycles were applied to generate cDNA and all samples underwent 15 or
762 16 cycles for final library generation. Libraries were sequenced on a NovaSeq 6000 S4 Flow Cell.
763 For UW cohort, the library was prepared following manufacturer's instructions and sequenced by
764 Northwest Genomics Services, University of Washington Genome Sciences on NovaSeq 6000
765 S2 Flow Cell.

766 Mouse scRNA-seq: Single cell suspensions were counted and adjusted to 1500 live cells per µl.
767 Approximately 20,000 cells per sample were loaded onto the Chromium controller. Libraries were
768 prepared according to manufacturer protocols (Chromium Next GEM Single Cell 3' Reagent Kits
769 v3.1 (Dual Index)). Sequencing was performed at Broad Institute on a NovaSeq 6000 SP Flow
770 Cell.

771

772 **Single cell data processing**

773 Human single-nucleus RNA-seq: FASTQs were demultiplexed and aligned to the human GRCh38
774 genome using CellRanger v6 (10X Genomics), counting reads mapping to pre-mRNA to account
775 for unspliced nuclear transcripts. Three approaches were combined for quality control: (1) ambient
776 RNA contamination was removed using SoupX[93] for each individual sample; (2) outliers with a
777 high ratio of mitochondrial (>10%, <200 features) relative to endogenous RNAs and homotypic
778 doublets (>5,000 features) were removed in Seurat[94]; and (3) doublets were removed using
779 DoubletFinder[95]. Nuclei with > 200 unique molecular identifiers were retained. The final dataset
780 contained 197,108 nuclei.

781 Datasets from ROSMAP and UW cohorts were combined and batch-corrected using Harmony
782 with default parameters. Cell type annotations were assigned based on canonical marker genes.

783 Mouse single-cell RNA-seq: Gene expression data were processed using CellRanger v8 with
784 alignment to the mm39 reference genome followed by removal of ambient RNA contamination
785 using CellBender v0.3.0[96]. We filtered cells with <300 detected features or >30% mitochondrial
786 reads, yielding a total of 87,948 cells. Batch effects between experimental days were corrected
787 using Harmony integration (lambda = 1).

788 Clustering was performed iteratively across at progressively refined resolutions to identify
789 and remove doublets and low-quality cells. Label transfer from an annotated reference dataset
790 was used to guide initial annotations[14]. Cell type annotations were assigned hierarchically at four
791 levels (Class, Type, Subtype, State) based on canonical marker genes: epithelial (*Htr2c*, *Wdr17*,
792 *Pcp4*, *Cd164*), fibroblast (*Coch*, *Dcn*), pericyte (*Notch3*, *Cox4i2*), smooth muscle cell (*Acta2*,
793 *Myh11*, *Tagln*), endothelial (*Pecam1*, *Cldn5*), macrophage (*Csf1r*, *Pf4*, *Cd163*, *Lgals3*, *Cadm1*),
794 microglia (*Siglech*), monocyte/DC (Ccr2*),* and lymphoid (*Cd3e*, *Cd8b1*, *Nkg7*, *Xcl1*).

795 Estimation of Variance

796 We performed variance decomposition using variancePartition[97] on sample-wise average
797 expression from the Harmony-integrated human object and fit linear mixed models with main
798 effects for feature counts, mitochondrial percentage, study, APOE genotype, age of death, sex,
799 Braak score, postmortem interval, Alzheimer's disease status, and tissue processing batch, plus
800 interaction terms (**Figure S1**).

801 Cell state taxonomy construction.

802 Hierarchical relationships among end-clusters in ChP cell types (cell "states") were
803 inferred using aggregated expression profiles, which were computed for each cell state across
804 highly variable genes using a median absolute deviation (MAD)-based threshold on residuals
805 from a loess-fitted mean-variance relationship. Expression profiles were z-scored across cell
806 states, Euclidean distances were computed, and hierarchical clustering was performed using
807 Ward's metric (ward.D2).

808 Differential cell state abundance

809 Differential abundance of cell states between AD and control subjects was assessed using
810 limma[98] with arcsin-square root transformed proportions. Donors with fewer than 300 total cells
811 were excluded to ensure robust proportion estimates. For each donor, the proportion of cells
812 belonging to each cell state was calculated, then proportions were arc-square root transformed
813 to stabilize variance and approximate normality. A linear model was fit with disease status with
814 study of origin (ROSMAP or UW) as a covariate: transformed proportion ~ AD_status + study.
815 Empirical Bayes moderation was applied using robust estimation. Log odds ratio were calculated
816 to quantify effect size, with positive values indicating enrichment in AD relative to Control, and p-
817 values were adjusted for multiple testing using the Benjamini-Hochberg FDR method.

818 Pseudobulk differential gene expression and gene set enrichment analysis

819 Differential gene expression between AD and Control was assessed using DESeq2[99] on
820 pseudobulk expression profiles, where raw counts were aggregated by summing across all cells
821 of a particular cell type belonging to each donor. Counts matrices were filtered to retain genes
822 detected in at least 30% of samples with expression in at least 5% of cells within the population.
823 The DESeq2 object was generated with the design formula: ~ AD_status + Age_scaled + Sex.
824 Gene set enrichment analysis (GSEA) was performed using fgsea[100] on DESeq2 results using
825 the Hallmark gene sets from msigdbr. Pathways with adjusted p-values < 0.05 were considered
826 significant.

827 Cell-Cell Communication Analysis

828 Intercellular communication was inferred using MultiNicheNet[47], which integrates
829 differential expression analysis with *a priori* knowledge of ligand-receptor and ligand-target
830 relationships. First, we excluded neural and glial cells (including microglia) and filtered cell types
831 with fewer than 10 cells per sample and present in fewer than 30% of samples within a disease
832 group. Next, we filtered genes that were detected in fewer than 5% of cells and fewer than 30%
833 of samples per condition. We then generated pseudobulk expression profiles per cell type per
834 sample for differential gene expression. For AD vs. Control differential interaction analysis (Figure

835 3), we used the contrast AD – Control and included study of origin as a covariate. For analysis of
836 differential ligand activity between AD, MCI, and Control, we set the contrast to AD –
837 (Control+MCI)/2, MCI – (AD+Control)/2, Control – (AD+MCI)/2. Genes with log2FC and $p<0.05$
838 were considered significant.

839 Ligand activity inference

840 For each receiver cell type, ligand activities were inferred based on the enrichment of
841 ligand target genes among differentially expressed genes. The NicheNet activity score reflects
842 the regulatory potential of each ligand to induce the observed transcriptional differences. The top
843 250 target genes per ligand were considered for activity scoring and only upregulated ligand
844 activities were retained.

845

846 **Pathological analysis of human choroid plexus**

847 Pathological procedures

848 1. Vantaa 85+ cohort: During the course of the study, brains harvested at autopsy were fixed for
849 at least two weeks in formalin before sampling. Neuropathological examination was performed
850 for all cases as described before[48-50]. Specimens of the right lateral ventricle ChP embedded in
851 paraffin were used for this study.

852 2. TSDS cohort: Individual tissue samples (cerebellar cortex, frontal cortex, hippocampus, insula-
853 putamen, pons, and substantia nigra) from unfixed brains were collected at forensic autopsy and
854 stored in phosphate-buffered 4% formaldehyde solution for at least 48 hours prior to paraffin
855 embedding into TissueTek cartridges[51-53].

856 3. UW cohort: UW AD Research Center (ADRC) Neuropathology Core handled tissue evaluation
857 and processing blind to clinical diagnosis as previously described[101-103]. Brain tissues used in this
858 study were immersion-fixed in 10% neutral buffered formalin for at least 2 weeks and evaluated
859 (wholly and after coronal sectioning) for any gross lesions. Tissue samples were dissected,
860 processed, and embedded in paraffin prior to sectioning and staining.

861
862 Anti-Iba1 immunohistochemistry

863 4 µm thick paraffin sections were mounted on glass slides and dried overnight at 37°C,
864 followed by incubation at 56°C for 30 min. - 1h. After automated deparaffinization (TissueTek
865 DRS, Sakura Finetek Europe B.V., Alphen aan den Rijn, the Netherlands) heat induced antigen
866 retrieval was performed at pH 6, for 20 min at 95 °C (Dako Target retrieval solution K2005, Agilent,
867 Santa Clara, CA, USA), followed by formic acid treatment for 5 mins (Fisher Chemical Formic
868 acid 98/100% Code: F/1900/PB15, Thermo Fisher Scientific, Waltham, MA, USA). Anti-Iba1
869 immunostaining (Wako polyclonal rabbit anti Iba1, #019-19741, FUJIFILM Biosciences, Santa
870 Ana, CA, USA; diluted at 1:1500 for 30 mins ([Dako AB diluent S2022, Agilent])), was carried out
871 on a Labvision Autostainer 480 (Thermo Fisher Scientific) using the Dako EnVision FLEX –kit
872 (K8002, Agilent). Counterstain was performed with Mayer's hematoxylin for 1-2 min.

873 Masson's Trichrome staining

874 Tissue sections (4 µm) were mounted on glass slides and dried overnight at 37 °C. The
875 next day, slides were incubated at 56 °C for 30 min before staining. Automated deparaffinization
876 and hydration (TissueTek DRS, Sakura Finetek Europe B.V., Alphen aan den Rijn, the
877 Netherlands) were performed prior to overnight fixation in Bouin's solution (HT10132, Sigma-
878 Aldrich, Saint Louis, USA) at RT followed by rinsing with tap water until clear. The slides were
879 stained with Weigert's Iron Hematoxylin (HT1079, Sigma-Aldrich, Saint Louis, USA) for 5 min
880 after which they were placed under running tap water for 5 min and rinsed with Aqua. The samples
881 were then stained with Biebrich Scarlet-Acid Fuchsin solution (HT151, Sigma-Aldrich, Saint Louis,
882 USA) for 5 min following aqua rinse 3 x 1 min. Next, the slides were incubated in Phosphotungstic
883 acid solution (HT152, Sigma-Aldrich, Saint Louis, USA) and Phosphomolybdic acid solution
884 (HT153, Sigma-Aldrich, Saint Louis, USA) in aqua (1:1:2) for 5 min following staining with Aniline
885 Blue solution (B8563, Sigma-Aldrich, Saint Louis, USA) for 5 min. To remove excess dye, the
886 sections were treated with 1 % acetic acid for 2 min followed by aqua rinse 3 x 1 min. The sections

887 were then dehydrated through a series of alcohols and cleared with xylene before applying
888 coverslips. Slide scanning was performed at FIMM Digital Microscopy and Molecular Pathology
889 Unit, Helsinki, Finland, on a Panoramic 250 Flash III (3D HISTECH, Budapest, Hungary).

890 Micro-CT

891 Samples (n=253 from Vantaa 85+ cohort) were scanned using a Quantum GX microCT
892 scanner (PerkinElmer, MA USA) with a peak voltage of 90 kV and a current of 88 µA. The imaging
893 was done in a 36 mm FOV with Cu 0.06+Al 0.5 X-ray filter and with ring reduction. High-resolution
894 scan mode was used with an exposure time of 4 min and a voxel size of 72 µm. The images were
895 captured over a 360° rotation around the sample. Tomograms were reconstructed with 3D Slicer
896 (version 5.6.1) software. ChP tissue was manually segmented from the cassette and surrounding
897 hippocampal tissue for the calcification volume analysis. Paraffin (and paraffin-infiltrated soft
898 tissue) was excluded from the volume analysis by setting a threshold. The mean Hounsfield Unit
899 (HU) value for paraffin was calculated from 10 different paraffin blocks that were manually
900 thresholded. The same threshold (-16 HU) was used for all samples within the cohort. An
901 estimation of the amount of calcification in each sample was calculated by dividing the acquired
902 calcification volume (mm^3) by an estimated tissue volume (mm^3). An estimate of the tissue volume
903 was calculated from the tissue area (Aiforia) and thickness of the tissue (3D slicer). Samples that
904 failed tissue recognition in Aiforia or had too little material left in the paraffin block were excluded
905 from the Micro-CT analysis.

906 Neuropathologic evaluation:

907 For the Vantaa 85+ study population, we used previously described Thal β-Amyloid phase,
908 Braak NFT stage[104] and Consortium to Establish a Registry for Alzheimer's Disease (CERAD)
909 neuritic plaque score[48] data.

910 AIFORIA analysis

911 We created an artificial intelligence model using Aiforia® Create version 6.4. (Aiforia
912 Technologies Oyj, Helsinki, Finland). The development of the convolutional neural network (CNN)

913 algorithm started by selecting 38 cases for training. Two training layers were created: ChP tissue
914 with area detection (parental layer) and another layer with object detection of villi (normal and
915 fibrotic) and psammoma bodies (child layers). The normal villi category included villi that had a
916 typical structure; epithelial cells lining the villus and a visible capillary, any villi with dense fibrosis
917 and missing capillary were annotated as fibrotic[34]. The psammoma body category included
918 calcified lamellar structures that often appeared in groups[105]. To set the ground truth, a total of
919 571 training regions (305 for ChP and 266 for the object classes) including background and
920 artifacts were annotated. The total number of object annotations was 6902 (2145 for psammoma
921 bodies, 2926 for normal villi and 1831 for fibrotic villi). Training parameters are shown in
922 **Supplemental Data 2**. The training resulted in a model with a total area error of 0.39 % (F1 score:
923 97.81 %) for the ChP tissue and a total object error of 5.64 % (F1 score: 97.15 %) for the object
924 classes. A visual pre-validation was carried out for a small set of cases from the TSDS, the Vantaa
925 85+, and the UW cohorts by the annotator. The Aiforia validation tool was used for the final
926 validation by three experienced neuropathologists (L.M., B.E., H.P.). For validation, four cases
927 that had not been used for training were selected. The external validators performed 18 area
928 annotations for the ChP tissue and 98 object annotations for the object classes on selected areas.
929 Among the three external validators, error for the ChP tissue was 6.52 % (F1 score: 91,43 %) and
930 for the object classes (villi and psammoma bodies) 0.67 % (F1 score: 99,66 %). Quantification of
931 the villi (normal and fibrotic) and psammoma bodies was carried out by image analysis with the
932 algorithm. The analysis also determined the area (mm^2) for ChP tissue in each sample. The
933 amount of fibrosis was calculated by dividing the number of fibrotic villi by the number of normal
934 villi and the number of psammoma bodies was divided by the tissue area. After running the image
935 analysis, manual quality check was performed on each sample. Samples that had poor tissue
936 recognition due to defective material or under 45 normal villi detected by the algorithm were
937 excluded from the analysis.

938 To analyze macrophages, we developed another CNN AI model for image analysis,
939 employing Aiforia® Create. At first, 50 cases were carefully selected for training. Specimens
940 obtained from the Helsinki Biobank were included to facilitate AI training on a heterogenous and
941 representative sample set. Segmentation was performed using two distinct training layers within
942 the training pipeline: A region layer for detection of the ChP and another region layer covering
943 different classes of macrophages (amoeboid, dystrophic, reactive, rod-shaped).

944 For training the algorithm, ChP macrophages were defined in resemblance to previously
945 published morphological descriptions of central nervous system microglia subtypes[106,107].
946 Representative micrographs of ChP macrophages are depicted in **Figure 3**.

947 1. Amoeboid macrophages show a rounded or oval, usually well delineated cell body with
948 smooth edges and no or only few, very short and stubby protrusions.
949 2. Dystrophic macrophages: Irregular cell body, with beaded/fragmented processes and
950 deteriorated cytoplasm. Borders might be hard to delineate.
951 3. Reactive macrophages: These show an enlarged cell body with marked, thickened
952 protrusions.
953 4. Rod-shaped macrophages: Thin, elongated rod- or club-shaped cell body, often found in
954 perivascular location, sometimes also appearing curvilinear, comma- or crescent-shaped.

955 A total of 774 training regions (278 for ChP and 496 for macrophage layers), including
956 tissue background and artifacts, were annotated to set a ground truth. Training parameters can
957 be found in **Supplemental Data 2**. Verification of the algorithm revealed a total area error for the
958 ChP layer of 0.01% (F1 score: 97.32%) and a total area error of 3.52% (F1 score: 89.12%) for
959 the macrophage layers. After yielding sufficient sensitivity and precision, validation of the
960 algorithm was carried out by i) visual pre-validation on a small subset of region of interest (ROI)
961 by the annotator and ii) using the Aiforia validation tool. Validation using Aiforia was performed
962 by three experienced pathologists (L.M., M.I.M., H.P.). For validation, eight cases with 51 regions
963 (16 ChP, 35 macrophages), not previously used for training were selected. Average total area

964 errors among the three validators were: 0.13% (ChP), 9.38% (macrophages), average F1 scores:
965 84.66% (ChP), 81.69% (macrophages).

966 For eventual quantification of ChP macrophages, a representative ChP ROI was marked
967 on scanned micrographs of anti-Iba1 immunostained slides. ROIs were selected so that most of
968 the ChP area with preserved histological architecture was included, whenever possible. As a
969 readout of the image analysis run, the ChP area as well as the ChP macrophage cell count and
970 % (area of macrophage class per total ChP area, termed "coverage" as of now) were determined
971 by the algorithm in Aiforia. A fraction of macrophages per sample (total sum of each macrophage
972 class divided by the total number of macrophages, in %) was calculated, in addition to the
973 coverage used in subsequent statistical analyses. Before and after running the algorithm, every
974 micrograph underwent a thorough quality check, particularly focusing on staining- and scanning
975 quality and assessing if the algorithm performed sufficiently, yielding 230 Vantaa 85+ and 59 UW
976 samples for further analysis.

977

978 **MRI scans of patients**

979 Image acquisition and analysis

980 20 7T T2*-gradient weighted echo (T2* GRE, TR/TE1/TE2/TE3/TE4/TI =
981 72.7/12.6/23.75/34.8/46.05/15ms, flip angle = 12°, 0.5mm isotropic) and 7T T1-weighted
982 magnetization prepared 2 rapid gradient echo (MP2RAGE, TR/TE/TI1/TI2 =
983 6,000/3.02/800/2,700ms, flip angle = 4/5°, 0.7mm isotropic) images were acquired on a Siemens
984 Magnetom scanner.

985 Quantitative susceptibility images were generated from 7T T2* GRE magnitude and phase
986 images. A brain mask was generated from the magnitude images using SynthStrip and eroded
987 by one voxel. Total-generalized-variation (TGV) based method for QSM reconstruction[108]
988 (available at: https://github.com/QSMxT/TGV_QSM) was applied to the phase image and

989 corresponding eroded brain mask for each echo. The four resulting QSM images were averaged
990 with 3DCalc in AFNI[109].

991 ChP was segmented on 7T T2* GRE magnitude images using 3D-Slicer
992 (https://www.slicer.org/)[110]. Segmentations were created in a semi-automated fashion by AAT by
993 applying the voxel thresholding tool dynamically to adequately segment the lateral ChP after
994 training (by S.V.O., neurologist with 7 years of experience in neuroimaging). Segmentations of
995 calcified regions were created by manually segmenting hypointense regions within the choroid
996 plexus on 7T T2* QSM **(Figure 2F)**. ChP and calcification volumes were recorded. The
997 calcification ratio (calcification volume divided by ChP volume) was calculated. The mean (±SD)
998 of QSM values of the ChP segmentations were recorded. The automated segmentation tool
999 Pseudo-Label Assisted nnU-Net (PLAn)[111] was applied to 7T T1-MP2RAGE images to identify
1000 CSF, gray matter (GM), white matter (WM), and white matter lesions (WML). Fractional GM (GM-
1001 F) and fractional CSF (CSF-F) were calculated by dividing GM and CSF volumes, respectively,
1002 by normalization to the total intracranial volume.

1003 Statistics

1004 Correlations were assessed with a Spearman correlation. Unpaired comparisons across
1005 categories were assessed with a Mann-Whitney U test. To account for age, a multiple linear
1006 regression model was performed.

1007 Cohort characteristics

Age (Mean ± SD)	47.35 ± 12.72 (n=20)
Sex (F/M)	16/4
Diagnoses (MS/OIND)	15/5
MS Subcategorization (RMS/PMS)	11/4
Treatment Status (On/Off or Naïve)	10/10
EDSS (Median, IQR)	3.0, 1.5-3.5 (n=15)
Scripps (Mean ± SD)	88.1 ± 9.8 (n=19)
PASAT (Mean ± SD)	54.2 ± 6.4 (n=11)
SDMT (Mean ± SD)	53.9 ± 10.2 (n=15)
GM-F (Mean ± SD)	0.458 ± 0.032(n=20)

WML (ml) (Mean ± SD)	3.88 ± 4.13 (n=20)
CSF-F (Mean ± SD)	0.193 ± 0.041 (n=20)
Calcification Ratio (Mean ± SD)	0.114 ± 0.077 (n=20)
CP Volume (ml) (Mean ± SD)	1.491 ± 0.452 (n=20)
CP QSM Susceptibility (ppm) (Mean ± SD)	-0.00120 ± 0.00793 (n=20)
Calcification Volume (ml) (Mean ± SD)	0.180 ± 0.153 (n=20)

1008

1009 **Spatial transcriptomics of human ChP**

1010 Xenium Sample Processing

1011 Postmortem human brain tissue was obtained from the Lieber Institute (Johns Hopkins
1012 University) and processed by the Knight Initiative for Brain Resilience (Stanford University), with
1013 approval from local ethics committees. Fresh frozen tissue sections were obtained from the lateral
1014 ventricle of a cognitively normal 48-year-old male donor. Sections were cut at 10 μm thickness
1015 using a cryostat and mounted on Xenium-compatible slides (10X Genomics). Slides were stored
1016 at −80 °C until processing.

1017 Xenium slides were processed according to the "Xenium *In Situ* for Fresh Frozen Tissues-
1018 Fixation & Permeabilization" demonstrated protocol (10x Genomics, CG000581), beginning with
1019 the 20-minute fixation step. Following permeabilization and cassette assembly, slides were
1020 processed according to the "Xenium *In Situ* Gene Expression with Cell Segmentation Staining
1021 User Guide" (10X Genomics, CG000749). Cell segmentation enables high–resolution cell
1022 boundary mapping. After hands-on slide processing, slides were loaded onto the Xenium
1023 Analyzer and processed.

1024 Spatial Transcriptomics Alignment, Quality Control, and Annotation

1025 A morphology stain (H&E) was applied to slides after the 10X Xenium workflow to assist
1026 with downstream spatial alignment and analysis. Images were processed and registered using
1027 Xenium Explorer v3.0.0, applying default autofluorescence correction and alignment parameters.
1028 Cells were retained for downstream analysis if they exhibited expression of at least ten transcripts

1029 distributed across a minimum of three distinct genes. Genes were retained if they were detected
1030 in greater than three cells. These filters were implemented in Scanpy (v.1.10.4)[112].

1031 Dimensionality reduction was conducted using scVI (v.1.2.0)[113], with two layers and 30-
1032 dimensional latent representation, applied to the integrated dataset. A categorical batch covariate
1033 was included during training to account for inter-run variability and to mitigate batch effects. The
1034 resulting latent representations underwent Leiden clustering. Cell type annotations were
1035 transferred from our human single-cell dataset via logistic regression using shared features.

1036 Spatial Neighborhood and Niche Analysis

1037 Computational inference of spatial niches was performed using an Adversarially
1038 Regularized Graph Variational Autoencoder (ARGVA)[114]. The encoder consisted of a two-layer
1039 Graph Convolutional Network (GCN) that takes gene expressions and adjacency matrices
1040 (constructed from cellular neighborhoods within a 100-unit radius) as inputs, then transforms them
1041 into latent representations, producing both point estimates and uncertainty values. The gene
1042 expression input consisted of log-normalized transcript counts restricted to the predefined Xenium
1043 gene panel.

1044 For decoding, we used an inner-product decoder for edge prediction to estimate the
1045 probability of two cells being within the same neighborhood[115]. To regularize the latent space and
1046 improve robustness, a discriminator neural network was used in an adversarial training
1047 framework, trained via logistic loss (a binary classification task). This adversarial regularization
1048 empirically improves both reconstruction fidelity and downstream clustering performance[114,115] .
1049 The objective function of our ARGVA combines (a) network reconstruction loss, (b) discriminator-
1050 derived regularization for noise-robust latent distributions, and (c) KL divergence to encourage
1051 alignment between the learned and prior distributions[116]. Model training was conducted over
1052 10,000 epochs. Leiden clustering was performed on the derived latent space using a resolution
1053 parameter of 0.05. Analysis for this section was performed using PyTorch (v.2.4.0) and PyTorch
1054 Geometric (v.2.5.3).

1055 The spatial colocalization of macrophages with other cell types was assessed by
1056 identifying the nearest cell type neighbor for each cell and calculating the relative frequencies of
1057 such proximities. These frequencies were normalized within each computationally defined niche
1058 to facilitate comparative analysis. This analysis was performed using custom scripts in Python
1059 (v.3.12.1).
1060

1061 **Mouse tissue collection and processing: explants and brain blocks**

1062 Animals were anesthetized by ketamine, perfused with ice cold PBS, and then followed
1063 by cold 4% paraformaldehyde (PFA). For cryosectioning, brains were dissected, further fixed in
1064 4% PFA at 4° C overnight, and then incubated in 30% sucrose for at least 48 hours, followed by
1065 OCT (1 hour on ice) prior to freezing by dry ice and 2-met-butane bath. For wholemount ChP
1066 explant, the LV ChPs were dissected and incubated in 4% PFA at room temperature for 5 min.,
1067 and then immunostained.
1068

1069 **Immunostaining of mouse samples**

1070 Cryosections and explants were blocked and permeabilized (0.3% Triton-X-100 in PBS;
1071 5% serum), incubated in primary antibodies overnight and secondary antibodies for 2 hours.
1072 Sections and explants were counterstained with Hoechst 33342 (Invitrogen H3570, 1:10,000) and
1073 mounted using Fluoromount-G (SouthernBiotech).

1074 The following primary antibodies were used: chicken anti-GFP (Abcam ab13970; 1:1000),
1075 rat anti-PECAM (BD Pharmingen 550274, 1:100), rat anti-CD45 (Fisher Scientific BDB550539,
1076 1:50), rabbit anti-Iba1 (Wako 019-19741, 1:200), goat Anti-Type IV Collagen-Alexa Fluor® 488
1077 (Southern Biotech 1340-30, 1:200), rabbit anti-Occludin (ThermoFisher 71-1500, 1:50), rabbit
1078 anti-Claudin 2 (ThermoFisher 51-6100, 1:100) Secondary antibodies were selected from the
1079 Alexa series (Invitrogen, 1:500).
1080

1081 **Confocal microscopy and image analysis**

1082 All confocal images were acquired using Zeiss LSM 880 and Zeiss LSM 980 with Airyscan
1083 confocal microscope. Explant images were taken with 2.5 µm z-stacks. All images were
1084 processed with FIJI[117].

1085

1086 **Headpost and cranial window placement**

1087 Mice used for *in vivo* two-photon imaging (4-6 months) were outfitted with a headpost and
1088 a 3 mm cranial window over the left lateral ventricle at least three weeks prior to imaging as
1089 previously described[14,55].

1090

1091 **Two-photon imaging and image processing**

1092 Two-photon microscopy (Olympus FVMPE-RS two-photon microscope; 512 x 512 pixels
1093 / frame) was used to record immune cells activities in ChP *in vivo* from 5xFAD mice or their WT
1094 littermate controls crossed with *Cx3cr1*^{GFP} (JAX 005582) mice or *Ccr2*^{GFP} (JAX 027619) mice. 200
1095 µm Z-stack was acquired with 5 µm stepping size at each field of view over the course of
1096 approximately 1 hour. Imaging and analyses were performed as described[14,55]. A 25X
1097 magnification, 8 mm working distance objective was used. Images were registered and processed
1098 following the established algorithm[14,55].

1099

1100 **Linearity index analysis of Occludin and Claudin 2**

1101 Individual cell borders were isolated in FIJI. The total length of the border was measured
1102 by manual tracing. The shortest distance was measured by drawing a straight line connecting the
1103 two ends of the border. Linearity index was calculated as Total length / straight line length

1104

1105 **Intracerebroventricular injection (ICV) of lipopolysaccharides (LPS)**

1106 Adult mice were anesthetized with isoflurane from a vaporizer. Following a midline scalp
1107 incision to expose the skull, the lateral ventricle was located by stereotaxic coordinates (bregma
1108 -0.4 mm, midline +1.0 mm, dura -2.2 mm). A single delivery path was prepared above the lateral
1109 ventricle. 5 µl of LPS solution (Sigma L3024, 0.5 mg/ml) was delivered using a Hamilton syringe
1110 into the lateral ventricle over the course of 5 min.
1111

1112 **HRP injection and TEM**

1113 As previously described[90], mice were weighed and injected retro-orbital under anesthesia
1114 (isoflurane vaporizer) with 0.5 mg horseradish peroxidase (HRP Sigma P8250-200 KU) per g
1115 bodyweight diluted in sterile PBS. HRP was diluted such that each mouse received 100uL per
1116 25 g bodyweight. HRP was allowed to circulate for 8 min, and then brains were harvested, frontal
1117 pole was removed, and fixed 1 hour in Karnovsky's fixative (5% glutaraldehyde, 4% PFA, 0.4%
1118 CaCl2, in 0.1 M cacodylate buffer - Electron Microscopy Sciences), then fixed in 4% PFA in 0.1 M
1119 cacodylate at 4 °C overnight on a shaker. After washing the brains thoroughly in 20 mM glycine
1120 followed by ice cold 0.1 M cacodylate buffer, the lateral ventricle ChP were dissected and
1121 processed for DAB (Millipore Sigma D5905). DAB solution was made using 5 mg DAB in 9 mL of
1122 0.1 M cacodylate plus ~9 mM H2O2. The ChP were developed at room temperature until dark
1123 brown (1-2 minutes). The ChP was then processed, sectioned, and imaged at the Conventional
1124 Electron Microscopy Facility at Harvard Medical School. Tissue was postfixed with 1%
1125 osmiumtetroxide (OsO4)/1.5% potassium ferrocyanide (KFeCN6) for one hour, washed in water
1126 three times and incubated in 1% aqueous uranyl acetate for one hour. This was followed by two
1127 washes in water and subsequent dehydration in grades of alcohol (10 min each; 50%, 70%, 90%,
1128 2 × 10 min 100%). Samples were then incubated in propyleneoxide for one hour and infiltrated
1129 overnight in a 1:1 mixture of propyleneoxide and TAAB Epon (Marivac Canada Inc. St. Laurent,
1130 Canada). The following day, the samples were embedded in TAAB Epon and polymerized at 60
1131 degrees C for 48 h. Ultrathin sections (about 80 nm) were cut on a Reichert Ultracut-S microtome,

1132 and picked up onto copper grids stained with lead citrate. Sections were examined in a JEOL
1133 1200EX Transmission electron microscope or a TecnaiG² Spirit BioTWIN. Images were recorded
1134 with an AMT 2k CCD camera.
1135

1136 **Multiplexed error-robust in situ hybridization (MERFISH): sample preparation and imaging**

1137 Mice were anesthetized and euthanized by decapitation. Brains were extracted and
1138 immediately transferred to cold OCT. Embedded brains were frozen and stored at -80°C. Vizgen's
1139 fresh frozen tissue sample preparation protocol was followed. Briefly, brains sections were sliced
1140 at 10 µm. Tissue slices were mounted on Vizgen's bead-coated functionalized coverslip. Once
1141 adhered to the coverslip, the samples were fixed (4% PFA in 1× PBS, 15 min, room temperature)
1142 and washed (3x, 5 min, 1X PBS). Then samples were incubated overnight in 70% EtOH to
1143 permeabilize the tissue. Following permeabilization samples were incubated for 30 min in
1144 Formamide Wash Buffer (30% deionized formamide (Sigma, S4117) in 2× SSC (Thermo Fisher,
1145 AM9765)) followed by the addition of the gene library mix for the hybridization step (48h, 37°C).
1146 Samples were then washed twice with Formamide Wash Buffer (2x, 30 min, 47°C), the tissue
1147 was embedded in a gel embedding solution (0.5% of 10% w/v ammonium persulfate, 0.05%
1148 TEMED, 4% 19:1 acrylamide/bis-acrylamide solution, 0.3M NaCl, 0.06M Tris PH8) followed by
1149 overnight incubation with tissue clearing solution (2X SSC, 2% SDS, 0.5% v/v Triton X-100, and
1150 proteinase K 1:100) at 37°C. Finally, tissue was washed, incubated with DAPI and polyT solution
1151 (15 min RT), and washed with formamide wash buffer (10 min RT). After sample preparation, the
1152 MERSCOPE 500 gene imaging kit was activated by adding 250 µl of Imaging Buffer Activator
1153 (VIZGEN, #203000015) and 100 µl of RNAse Inhibitor (New England BioLabs, M0314L). 15 ml of
1154 mineral oil was overlaid on top of the imaging buffer through the activation port and the instrument
1155 was primed and the imaging chamber was assembled as per MERSCOPE user guide. A 10x low
1156 resolution mosaic of the sample was then acquired, the imaging area was selected, and the
1157 sample was imaged.

1158

1159 **MERFISH post-imaging data processing and analysis**

1160 Following image acquisition, the resulting data were decoded using Vizgen's analyzing
1161 pipeline incorporated in the MERSCOPE. Vizgen's postprocessing tool (Vizgen, Cambridge, MA)
1162 was then applied to obtain the cell segmentation based on the DAPI staining by using the
1163 CellPose algorithm. Segmentation was performed on the middle Z plane (3rd out of 7) and cell
1164 borders were propagated to z-planes above and below. MERFISH processed data were analyzed
1165 in RStudio using Seurat 4.1.3, R 4.2.2 and custom-made scripts. Cell filtering was applied to the
1166 dataset to remove cells <100 μm^3 and <10 unique transcripts and <40 transcript counts. Cell gene
1167 expression per cell was then normalized to each cell's volume and the mean RNA per sample.
1168 Following annotation of choroid plexus (ChP) by region, ChP cells were subclustered and
1169 annotated by cell type using known marker genes. To assess differences in senescence gene
1170 expression across genotypes and cell types, we subset ChP cells by major cell type (Epithelial,
1171 Mesenchymal, Endothelial, & Immune) and compared senescence scores between wild-type
1172 (WT) and 5xFAD animals using the Wilcoxon rank-sum test. Senescence is evaluated by a set of
1173 genes from the recently published SenMayo[59] signature. Effect sizes were calculated using
1174 Cohen's d (effsize v0.8.1). P-values were adjusted across cell types using the Benjamini-
1175 Hochberg method to control the false discovery rate. Visualization of the SenMayo gene modules
1176 in WT and 5xFAD ChP was performed on the Vizgen MERSCOPE Visualizer software.

1177

1178 **Computational analysis, statistics and schematics**

1179 All single-cell RNA-seq analyses were performed in R (v4.5.1). Single-cell data processing
1180 utilized Seurat (v5.3.1)[94] with harmony (v1.2.4)[45] for batch correction. Differential cell type
1181 abundance was assessed using speckle (v1.10.0)[118] with limma (v3.66.0)[98], adjusting for study
1182 as a covariate. Pseudobulk differential expression analysis employed DESeq2 (v1.50.2)[99].
1183 Pathway enrichment analysis used fgsea (v1.36.0)[100] with gene sets from MSigDB (msigdbr

1184 v25.1.1), and gene signature scoring was performed using AUCell (v1.32.0)[119]. Cell-cell
1185 communication analysis employed multinichenetr (v2.1.0)[47]. Figures were generated using
1186 ComplexHeatmap (v2.26.0)[120] and circlize (v0.4.17)[121] for circos plots. Two-photon imaging data
1187 were processed with MATLAB pipelines as published and available on GitHub[14,55]. Statistical tests
1188 are specified in the respective sections in Methods. Schematic diagrams were created in parts
1189 with BioRender.com. Xenium visualization was performed using Matplotlib (v3.9.2) and Seaborn
1190 (v0.13.2)[122].

1191 **REFERENCES**

1192 1. Lun, M.P., Monuki, E.S., and Lehtinen, M.K. (2015). Development and functions of the
1193 choroid plexus–cerebrospinal fluid system. Nat Rev Neurosci *16*, 445–457.
1194 10.1038/nrn3921.
1195 2. Saunders, N.R., Dziegielewska, K.M., Fame, R.M., Lehtinen, M.K., and Liddelow, S.A.
1196 (2023). The choroid plexus: a missing link in our understanding of brain development and
1197 function. Physiol Rev *103*, 919–956. 10.1152/physrev.00060.2021.
1198 3. Ghersi-Egea, J.F., Strazielle, N., Catala, M., Silva-Vargas, V., Doetsch, F., and
1199 Engelhardt, B. (2018). Molecular anatomy and functions of the choroidal blood-
1200 cerebrospinal fluid barrier in health and disease. Acta Neuropathol *135*, 337–361.
1201 10.1007/s00401-018-1807-1.
1202 4. Fagan, A.M., and Holtzman, D.M. (2010). Cerebrospinal fluid biomarkers of Alzheimer's
1203 disease. Biomark Med *4*, 51–63. 10.2217/BMM.09.83.
1204 5. Fagan, A.M., Mintun, M.A., Mach, R.H., Lee, S.Y., Dence, C.S., Shah, A.R., LaRossa,
1205 G.N., Spinner, M.L., Klunk, W.E., Mathis, C.A., et al. (2006). Inverse relation between in
1206 vivo amyloid imaging load and cerebrospinal fluid Abeta42 in humans. Ann Neurol *59*,
1207 512–519. 10.1002/ana.20730.
1208 6. Fagan, A.M., Roe, C.M., Xiong, C., Mintun, M.A., Morris, J.C., and Holtzman, D.M. (2007).
1209 Cerebrospinal fluid tau/beta-amyloid(42) ratio as a prediction of cognitive decline in
1210 nondemented older adults. Arch Neurol *64*, 343–349. 10.1001/archneur.64.3.noc60123.
1211 7. Selkoe, D.J., and Hardy, J. (2016). The amyloid hypothesis of Alzheimer's disease at 25
1212 years. EMBO Mol Med *8*, 595–608. 10.15252/emmm.201606210.
1213 8. Butovsky, O., Rosenzweig, N., Kleemann, K.L., Jorfi, M., Kuchroo, V.K., Tanzi, R.E., and
1214 Weiner, H.L. (2025). Immune dysfunction in Alzheimer disease. Nat Rev Neurosci.
1215 10.1038/s41583-025-00997-0.
1216 9. Castellani, G., Croese, T., Peralta Ramos, J.M., and Schwartz, M. (2023). Transforming
1217 the understanding of brain immunity. Science *380*. 10.1126/science.abo7649.
1218 10. Gate, D., Saligrama, N., Leventhal, O., Yang, A.C., Unger, M.S., Middeldorp, J., Chen, K.,
1219 Lehallier, B., Channappa, D., De Los Santos, M.B., et al. (2020). Clonally expanded CD8
1220 T cells patrol the cerebrospinal fluid in Alzheimer's disease. Nature *577*, 399–404.
1221 10.1038/s41586-019-1895-7.
1222 11. Piehl, N., van Olst, L., Ramakrishnan, A., Teregulova, V., Simonton, B., Zhang, Z., Tapp,
1223 E., Channappa, D., Oh, H., Losada, P.M., et al. (2022). Cerebrospinal fluid immune
1224 dysregulation during healthy brain aging and cognitive impairment. Cell *185*, 5028–5039
1225 e5013. 10.1016/j.cell.2022.11.019.
1226 12. Courtney, Y., Head, J.P., Dani, N., Chechneva, O.V., Shipley, F.B., Zhang, Y., Holtzman,
1227 M.J., Sadegh, C., Libermann, T.A., and Lehtinen, M.K. (2025). Choroid plexus apocrine
1228 secretion shapes CSF proteome during mouse brain development. Nat Neurosci *28*,
1229 1446–1459. 10.1038/s41593-025-01972-9.
1230 13. Lehtinen, M.K., Zappaterra, M.W., Chen, X., Yang, Y.J., Hill, A.D., Lun, M., Maynard, T.,
1231 Gonzalez, D., Kim, S., Ye, P., et al. (2011). The cerebrospinal fluid provides a proliferative
1232 niche for neural progenitor cells. Neuron *69*, 893–905. 10.1016/j.neuron.2011.01.023.
1233 14. Xu, H., Lotfy, P., Gelb, S., Pragana, A., Hehnly, C., Byer, L.I.J., Shipley, F.B., Zawadzki,
1234 M.E., Cui, J., Deng, L., et al. (2024). The choroid plexus synergizes with immune cells
1235 during neuroinflammation. Cell *187*, 4946–4963 e4917. 10.1016/j.cell.2024.07.002.
1236 15. Silva-Vargas, V., Maldonado-Soto, A.R., Mizrak, D., Codega, P., and Doetsch, F. (2016).
1237 Age-Dependent Niche Signals from the Choroid Plexus Regulate Adult Neural Stem Cells.
1238 Cell Stem Cell *19*, 643–652. 10.1016/j.stem.2016.06.013.

16. Tsitsou-Kampeli, A., Suzzi, S., and Schwartz, M. (2024). The immune and metabolic milieu of the choroid plexus as a potential target in brain protection. Trends Neurosci *47*, 573–582. 10.1016/j.tins.2024.05.010.
17. Kipnis, J., Benveniste, H., Eichmann, A., Thomas, J.L., Reich, D.S., Lewis, L.D., Tsai, L.H., Drieu, A., Bakker, E., Kelley, D.H., et al. (2025). Resolving the mysteries of brain clearance and immune surveillance. Neuron *113*, 3908–3923. 10.1016/j.neuron.2025.10.036.
18. Carna, M., Onyango, I.G., Katina, S., Holub, D., Novotny, J.S., Nezvedova, M., Jha, D., Nedelska, Z., Lacovich, V., Vyvere, T.V., et al. (2023). Pathogenesis of Alzheimer's disease: Involvement of the choroid plexus. Alzheimers Dement *19*, 3537–3554. 10.1002/alz.12970.
19. Lin, M., Zeng, Q., Zhong, S., Nie, S., Zhang, R., Hong, H., Liu, L., Wang, S., Li, K., Luo, X., et al. (2025). Association Between Choroid Plexus Morphological Alterations, Alzheimer Pathologies, and Cognitive Impairment: A Longitudinal Study. Neurology *105*, e213953. 10.1212/WNL.0000000000213953.
20. Stopa, E.G., Tanis, K.Q., Miller, M.C., Nikonova, E.V., Podtelezhnikov, A.A., Finney, E.M., Stone, D.J., Camargo, L.M., Parker, L., Verma, A., et al. (2018). Comparative transcriptomics of choroid plexus in Alzheimer's disease, frontotemporal dementia and Huntington's disease: implications for CSF homeostasis. Fluids Barriers CNS *15*, 18. 10.1186/s12987-018-0102-9.
21. Tijms, B.M., Vromen, E.M., Mjaavatten, O., Holstege, H., Reus, L.M., van der Lee, S., Wesenhagen, K.E.J., Lorenzini, L., Vermunt, L., Venkatraghavan, V., et al. (2024). Cerebrospinal fluid proteomics in patients with Alzheimer's disease reveals five molecular subtypes with distinct genetic risk profiles. Nat Aging *4*, 33–47. 10.1038/s43587-023-00550-7.
22. Yang, A.C., Kern, F., Losada, P.M., Agam, M.R., Maat, C.A., Schmartz, G.P., Fehlmann, T., Stein, J.A., Schaum, N., Lee, D.P., et al. (2021). Dysregulation of brain and choroid plexus cell types in severe COVID-19. Nature *595*, 565–571. 10.1038/s41586-021-03710-0.
23. Zhu, L., Stein, L.R., Kim, D., Ho, K., Yu, G.Q., Zhan, L., Larsson, T.E., and Mucke, L. (2018). Klotho controls the brain-immune system interface in the choroid plexus. Proc Natl Acad Sci U S A *115*, E11388–E11396. 10.1073/pnas.1808609115.
24. Alicioglu, B., Yilmaz, G., Tosun, O., and Bulakbasi, N. (2017). Diffusion-weighted magnetic resonance imaging in the assessment of choroid plexus aging. Neuroradiol J *30*, 490–495. 10.1177/1971400917714280.
25. Baruch, K., Deczkowska, A., David, E., Castellano, J.M., Miller, O., Kertser, A., Berkutzki, T., Barnett-Itzhaki, Z., Bezalel, D., Wyss-Coray, T., et al. (2014). Aging. Aging-induced type I interferon signaling at the choroid plexus negatively affects brain function. Science (New York, N.Y.) *346*, 89–93. 10.1126/science.1252945.
26. Daneman, R. (2012). The blood-brain barrier in health and disease. Ann Neurol *72*, 648–672. 10.1002/ana.23648.
27. Zenaro, E., Piacentino, G., and Constantin, G. (2017). The blood-brain barrier in Alzheimer's disease. Neurobiol Dis *107*, 41–56. 10.1016/j.nbd.2016.07.007.
28. Dani, N., Herbst, R.H., McCabe, C., Green, G.S., Kaiser, K., Head, J.P., Cui, J., Shipley, F.B., Jang, A., Dionne, D., et al. (2021). A cellular and spatial map of the choroid plexus across brain ventricles and ages. Cell *184*, 3056–3074 e3021. 10.1016/j.cell.2021.04.003.
29. Xu, H., Hehnly, C., and Lehtinen, M.K. (2025). The choroid plexus: a command center for brain-body communication during inflammation. Curr Opin Immunol *93*, 102540. 10.1016/j.coi.2025.102540.
30. Courtney, Y., Hochstetler, A., and Lehtinen, M.K. (2024). Choroid Plexus Pathophysiology. Annu Rev Pathol. 10.1146/annurev-pathmechdis-051222-114051.

31. Engelhardt, B., Wolburg-Buchholz, K., and Wolburg, H. (2001). Involvement of the choroid plexus in central nervous system inflammation. Microsc Res Tech *52*, 112–129. doi:10.1002/1097-0029(20010101)52:1<112::AID-JEMT13>3.0.CO;2-5.
32. Serot, J.-M., Béné, M.-C., and Faure, G.C. (2003). Choroid plexus, aging of the brain, and Alzheimer's disease. Frontiers in bioscience. *8*, s515–s521. 10.2741/1085.
33. Saul, J., Hutchins, E., Reiman, R., Saul, M., Ostrow, L.W., Harris, B.T., Van Keuren-Jensen, K., Bowser, R., and Bakkar, N. (2020). Global alterations to the choroid plexus blood-CSF barrier in amyotrophic lateral sclerosis. Acta Neuropathol Commun *8*, 92. 10.1186/s40478-020-00968-9.
34. Prineas, J.W., Parratt, J.D., and Kirwan, P.D. (2016). Fibrosis of the Choroid Plexus Filtration Membrane. J Neuropathol Exp Neurol *75*, 855–867. 10.1093/jnen/nlw061.
35. Kiktenko, A.I. (1986). Biondi bodies in the choroid plexus epithelium of the human brain. A scanning electron-microscopic study. Cell Tissue Res *244*, 239–240. 10.1007/BF00218405.
36. Wen, G.Y., Wisniewski, H.M., and Kascsak, R.J. (1999). Biondi ring tangles in the choroid plexus of Alzheimer's disease and normal aging brains: a quantitative study. Brain Res *832*, 40–46. 10.1016/s0006-8993(99)01466-3.
37. Choi, J.D., Moon, Y., Kim, H.J., Yim, Y., Lee, S., and Moon, W.J. (2022). Choroid Plexus Volume and Permeability at Brain MRI within the Alzheimer Disease Clinical Spectrum. Radiology *304*, 635–645. 10.1148/radiol.212400.
38. Novakova Martinkova, J., Ferretti, M.T., Ferrari, A., Lerch, O., Matuskova, V., Secnik, J., Hort, J., and Alzheimer's Disease Neuroimaging, I. (2023). Longitudinal progression of choroid plexus enlargement is associated with female sex, cognitive decline and ApoE E4 homozygote status. Front Psychiatry *14*, 1039239. 10.3389/fpsyt.2023.1039239.
39. Ozsahin, I., Wang, X., Zhou, L., Xi, K., Hojjati, S.H., Tanzi, E., Maloney, T., Fung, E.K., Dyke, J.P., Chen, K., et al. (2025). Divergent neurodegeneration associations with choroid plexus volume and degree of calcification in cognitively normal APOE epsilon4 carriers and non-carriers. Sci Rep *15*, 12818. 10.1038/s41598-025-97409-1.
40. Xia, H., Feng, Y., Zhu, H., Yang, D., Wang, C., Wang, Z., Zhang, H., Pan, W., Zhao, Y., Alzheimer's Disease Neuroimaging, I., et al. (2025). Association of choroid plexus volume with white matter microstructure, glymphatic function, and peripheral systemic inflammation in Alzheimer's disease. Transl Psychiatry *15*, 238. 10.1038/s41398-025-03432-1.
41. Delvenne, A., Vandendriessche, C., Gobom, J., Burgelman, M., Dujardin, P., De Nolf, C., Tijms, B.M., Teunissen, C.E., Schindler, S.E., Verhey, F., et al. (2024). Involvement of the choroid plexus in Alzheimer's disease pathophysiology: findings from mouse and human proteomic studies. Fluids Barriers CNS *21*, 58. 10.1186/s12987-024-00555-3.
42. Philippe, T.J., Avey, D.R., Kearns, N.A., Vyas, H., Tissera, S., Xu, J., Ng, B., Saunders, D.M., Lagrimas, A.K., Duong, D., et al. (2025). A Multi-omic Atlas of Human Choroid Plexus in Alzheimer's Disease. bioRxiv. 10.1101/2025.11.23.690014.
43. Yan, Z.J., Ye, M., Li, J., Zhang, D.F., and Yao, Y.G. (2025). Early transcriptional and cellular abnormalities in choroid plexus of a mouse model of Alzheimer's disease. Mol Neurodegener *20*, 62. 10.1186/s13024-025-00853-w.
44. Oakley, H., Cole, S.L., Logan, S., Maus, E., Shao, P., Craft, J., Guillozet-Bongaarts, A., Ohno, M., Disterhoft, J., Van Eldik, L., et al. (2006). Intraneuronal beta-amyloid aggregates, neurodegeneration, and neuron loss in transgenic mice with five familial Alzheimer's disease mutations: potential factors in amyloid plaque formation. J Neurosci *26*, 10129–10140. 10.1523/JNEUROSCI.1202-06.2006.
45. Korsunsky, I., Millard, N., Fan, J., Slowikowski, K., Zhang, F., Wei, K., Baglaenko, Y., Brenner, M., Loh, P.R., and Raychaudhuri, S. (2019). Fast, sensitive and accurate

integration of single-cell data with Harmony. Nat Methods *16*, 1289–1296. 10.1038/s41592-019-0619-0.

46. Hutchins, A.P., Poulain, S., and Miranda-Saavedra, D. (2012). Genome-wide analysis of STAT3 binding in vivo predicts effectors of the anti-inflammatory response in macrophages. Blood *119*, e110–119. 10.1182/blood-2011-09-381483.
47. Browaeys, R., Gilis, J., Sang-Aram, C., De Bleser, P., Hoste, L., Tavernier, S., Lambrechts, D., Seurinck, R., and Saeys, Y. (2023). MultiNicheNet: a flexible framework for differential cell-cell communication analysis from multi-sample multi-condition single-cell transcriptomics data. bioRxiv, 2023.2006.2013.544751. 10.1101/2023.06.13.544751.
48. Polvikoski, T., Sulkava, R., Myllykangas, L., Notkola, I.L., Niinisto, L., Verkkoniemi, A., Kainulainen, K., Kontula, K., Perez-Tur, J., Hardy, J., and Haltia, M. (2001). Prevalence of Alzheimer's disease in very elderly people: a prospective neuropathological study. Neurology *56*, 1690–1696. 10.1212/wnl.56.12.1690.
49. Polvikoski, T., Sulkava, R., Rastas, S., Sutela, A., Niinisto, L., Notkola, I.L., Verkkoniemi, A., Viramo, P., Juva, K., and Haltia, M. (2006). Incidence of dementia in very elderly individuals: a clinical, neuropathological and molecular genetic study. Neuroepidemiology *26*, 76–82. 10.1159/000090252.
50. Tanskanen, M., Makela, M., Notkola, I.L., Myllykangas, L., Rastas, S., Oinas, M., Lindsberg, P.J., Polvikoski, T., Tienari, P.J., and Paetau, A. (2017). Population-based analysis of pathological correlates of dementia in the oldest old. Ann Clin Transl Neurol *4*, 154–165. 10.1002/acn3.389.
51. Karhunen, P., Tuomisto, S., Goebeler, S., Martiskainen, M., and Kok, E. (2025). Common occurrence of atrophic gastritis in an ageing non-hospitalised population: an autopsy study. Age Ageing *54*. 10.1093/ageing/afaf047.
52. Kok, E.H., Paetau, A., Martiskainen, M., Lyytikainen, L.P., Lehtimaki, T., Karhunen, P., and Myllykangas, L. (2024). Accumulation of Lewy-Related Pathology Starts in Middle Age: The Tampere Sudden Death Study. Ann Neurol *95*, 843–848. 10.1002/ana.26912.
53. Tuomisto, S., Huhtala, H., Martiskainen, M., Goebeler, S., Lehtimaki, T., and Karhunen, P.J. (2019). Age-dependent association of gut bacteria with coronary atherosclerosis: Tampere Sudden Death Study. PLoS One *14*, e0221345. 10.1371/journal.pone.0221345.
54. Zhou, X., Franklin, R.A., Adler, M., Jacox, J.B., Bailis, W., Shyer, J.A., Flavell, R.A., Mayo, A., Alon, U., and Medzhitov, R. (2018). Circuit Design Features of a Stable Two-Cell System. Cell *172*, 744–757 e717. 10.1016/j.cell.2018.01.015.
55. Shipley, F.B., Dani, N., Xu, H., Deister, C., Cui, J., Head, J.P., Sadegh, C., Fame, R.M., Shannon, M.L., Flores, V.I., et al. (2020). Tracking Calcium Dynamics and Immune Surveillance at the Choroid Plexus Blood-Cerebrospinal Fluid Interface. Neuron *108*, 623–639 e610. 10.1016/j.neuron.2020.08.024.
56. Andersson, E., Janelidze, S., Lampinen, B., Nilsson, M., Leuzy, A., Stomrud, E., Blennow, K., Zetterberg, H., and Hansson, O. (2020). Blood and cerebrospinal fluid neurofilament light differentially detect neurodegeneration in early Alzheimer's disease. Neurobiol Aging *95*, 143–153. 10.1016/j.neurobiolaging.2020.07.018.
57. Andersson, E., Lindblom, N., Janelidze, S., Salvado, G., Gkanatsiou, E., Soderberg, L., Moller, C., Lannfelt, L., Ge, J., Hanrieder, J., et al. (2025). Soluble cerebral Abeta protofibrils link Abeta plaque pathology to changes in CSF Abeta(42)/Abeta(40) ratios, neurofilament light and tau in Alzheimer's disease model mice. Nat Aging *5*, 366–375. 10.1038/s43587-025-00810-8.
58. Chen, Y., Zhou, Y., Bai, Y., Jia, K., Zhang, H., Chen, Q., Song, M., Dai, Y., Shi, J., Chen, Z., et al. (2025). Macrophage-derived CTSS drives the age-dependent disruption of the blood-CSF barrier. Neuron *113*, 1082–1097 e1088. 10.1016/j.neuron.2025.01.023.
59. Saul, D., Kosinsky, R.L., Atkinson, E.J., Doolittle, M.L., Zhang, X., LeBrasseur, N.K., Pignolo, R.J., Robbins, P.D., Niedernhofer, L.J., Ikeno, Y., et al. (2022). A new gene set

1391 identifies senescent cells and predicts senescence-associated pathways across tissues.
1392 Nat Commun *13*, 4827. 10.1038/s41467-022-32552-1.
1393 60. Suryadevara, V., Hudgins, A.D., Rajesh, A., Pappalardo, A., Karpova, A., Dey, A.K.,
1394 Hertzel, A., Agudelo, A., Rocha, A., Soygur, B., et al. (2024). SenNet recommendations
1395 for detecting senescent cells in different tissues. Nat Rev Mol Cell Biol *25*, 1001–1023.
1396 10.1038/s41580-024-00738-8.
1397 61. Wu, Q., Klopack, E.T., Kim, J.K., Arpawong, T.E., Thyagarajan, B., Cole, S., Faul, J.D.,
1398 Zhou, F., and Crimmins, E.M. (2025). Gene expression composite scores of cellular
1399 senescence predict aging health outcomes in the Health and Retirement Study. Nat
1400 Commun *16*, 9044. 10.1038/s41467-025-64835-8.
1401 62. Huynh, T.V., Wang, C., Tran, A.C., Tabor, G.T., Mahan, T.E., Francis, C.M., Finn, M.B.,
1402 Spellman, R., Manis, M., Tanzi, R.E., et al. (2019). Lack of hepatic apoE does not influence
1403 early Abeta deposition: observations from a new APOE knock-in model. Mol
1404 Neurodegener *14*, 37. 10.1186/s13024-019-0337-1.
1405 63. Wang, C., Xiong, M., Gratuze, M., Bao, X., Shi, Y., Andhey, P.S., Manis, M., Schroeder,
1406 C., Yin, Z., Madore, C., et al. (2021). Selective removal of astrocytic APOE4 strongly
1407 protects against tau-mediated neurodegeneration and decreases synaptic phagocytosis
1408 by microglia. Neuron *109*, 1657–1674 e1657. 10.1016/j.neuron.2021.03.024.
1409 64. Umemura, Y., Watanabe, K., Kasai, S., Ide, S., Ishimoto, Y., Sasaki, M., Nagaya, H.,
1410 Tatsuo, S., Mikami, T., Tamada, Y., et al. (2024). Choroid plexus enlargement in mild
1411 cognitive impairment on MRI: a large cohort study. Eur Radiol *34*, 5297–5304.
1412 10.1007/s00330-023-10572-9.
1413 65. Li, J., Gao, Y., Xu, Y., Dai, W., Hu, Y., Feng, X., Wu, D., Zhao, L., Alzheimer's Disease
1414 Neuroimaging, I., and the Parkinson's Progression Markers, I. (2025). Morphological
1415 changes of the choroid plexus in the lateral ventricle across the lifespan: 5551 subjects
1416 from fetus to elderly. Neuroimage *318*, 121392. 10.1016/j.neuroimage.2025.121392.
1417 66. Tahira, A., Marques, F., Lisboa, B., Feltrin, A., Barbosa, A., de Oliveira, K.C., de Braganca
1418 Pereira, C.A., Leite, R., Grinberg, L., Suemoto, C., et al. (2021). Are the 50's, the transition
1419 decade, in choroid plexus aging? Geroscience *43*, 225–237. 10.1007/s11357-021-00329-
1420 x.
1421 67. Alisch, J.S.R., Kiely, M., Triebswetter, C., Alsameen, M.H., Gong, Z., Khattar, N., Egan,
1422 J.M., and Bouhrara, M. (2021). Characterization of Age-Related Differences in the Human
1423 Choroid Plexus Volume, Microstructural Integrity, and Blood Perfusion Using
1424 Multiparameter Magnetic Resonance Imaging. Front Aging Neurosci *13*, 734992.
1425 10.3389/fnagi.2021.734992.
1426 68. Sun, Z., Li, C., Zhang, J., Wisniewski, T., and Ge, Y. (2024). Choroid plexus aging:
1427 structural and vascular insights from the HCP-aging dataset. Fluids Barriers CNS *21*, 98.
1428 10.1186/s12987-024-00603-y.
1429 69. Green, G.S., Fujita, M., Yang, H.S., Taga, M., Cain, A., McCabe, C., Comandante-Lou,
1430 N., White, C.C., Schmidtner, A.K., Zeng, L., et al. (2024). Cellular communities reveal
1431 trajectories of brain ageing and Alzheimer's disease. Nature *633*, 634–645.
1432 10.1038/s41586-024-07871-6.
1433 70. Hitpass Romero, K., Stevenson, T.J., Smyth, L.C.D., Watkin, B., McCullough, S.J.C.,
1434 Vinnell, L., Smith, A.M., Schweder, P., Correia, J.A., Kipnis, J., et al. (2025). Age-related
1435 meningeal extracellular matrix remodeling compromises CNS lymphatic function. J
1436 Neuroinflammation *22*, 109. 10.1186/s12974-025-03436-0.
1437 71. Murakami, R., Chiba, Y., Miyatake, N., Miyai, Y., Matsumoto, K., Wakamatsu, K., Saito,
1438 Y., Hara, M., Murayama, S., and Ueno, M. (2025). Morphometry of choroid plexus
1439 epithelial cells in neurodegenerative diseases. Neuropathology *45*, 202–209.
1440 10.1111/neup.13019.

1441 72. Kant, S., Stopa, E.G., Johanson, C.E., Baird, A., and Silverberg, G.D. (2018). Choroid
1442 plexus genes for CSF production and brain homeostasis are altered in Alzheimer's
1443 disease. Fluids Barriers CNS *15*, 34. 10.1186/s12987-018-0120-7.
1444 73. May, C., Kaye, J.A., Atack, J.R., Schapiro, M.B., Friedland, R.P., and Rapoport, S.I.
1445 (1990). Cerebrospinal fluid production is reduced in healthy aging. Neurology *40*, 500–
1446 503. 10.1212/wnl.40.3_part_1.500.
1447 74. Dorrier, C.E., Jones, H.E., Pintaric, L., Siegenthaler, J.A., and Daneman, R. (2022).
1448 Emerging roles for CNS fibroblasts in health, injury and disease. Nat Rev Neurosci *23*,
1449 23–34. 10.1038/s41583-021-00525-w.
1450 75. Ewing-Crystal, N.A., Mroz, N.M., Larpthaveesarp, A., Lizama, C.O., Pennington, R.,
1451 Chiaranunt, P., Dennis, J.I., Chang, A.A., Merrill, E.D., Caryotakis, S.E., et al. (2025).
1452 Dynamic fibroblast-immune interactions shape recovery after brain injury. Nature *646*,
1453 934–944. 10.1038/s41586-025-09449-2.
1454 76. Xue, X., Wu, X., Fan, Y., Han, S., Zhang, H., Sun, Y., Yin, Y., Yin, M., Chen, B., Sun, Z.,
1455 et al. (2024). Heterogeneous fibroblasts contribute to fibrotic scar formation after spinal
1456 cord injury in mice and monkeys. Nat Commun *15*, 6321. 10.1038/s41467-024-50564-x.
1457 77. Drieu, A., Du, S., Storck, S.E., Rustenhoven, J., Papadopoulos, Z., Dykstra, T., Zhong, F.,
1458 Kim, K., Blackburn, S., Mamuladze, T., et al. (2022). Parenchymal border macrophages
1459 regulate the flow dynamics of the cerebrospinal fluid. Nature *611*, 585–593.
1460 10.1038/s41586-022-05397-3.
1461 78. Ocanas, S.R., Pham, K.D., Cox, J.E.J., Keck, A.W., Ko, S., Ampadu, F.A., Porter, H.L.,
1462 Ansere, V.A., Kulpa, A., Kellogg, C.M., et al. (2023). Microglial senescence contributes to
1463 female-biased neuroinflammation in the aging mouse hippocampus: implications for
1464 Alzheimer's disease. J Neuroinflammation *20*, 188. 10.1186/s12974-023-02870-2.
1465 79. Kaiser, K., Silva-Vargas, V., von Allmen, L., Sakoparnig, T., and Doetsch, F. (2025).
1466 Choroid plexus sex differences in secretory signalling and immune compartments.
1467 bioRxiv, 2025.2008.2015.670566. 10.1101/2025.08.15.670566.
1468 80. Masters, H., Wang, S., Tu, C., Nguyen, Q., Sha, Y., Karikomi, M.K., Fung, P.S.R., Tran,
1469 B., Martel, C., Kwang, N., et al. (2025). Sequential emergence and contraction of epithelial
1470 subtypes in the prenatal human choroid plexus revealed by a stem cell model. Nat
1471 Commun *16*, 5149. 10.1038/s41467-025-60361-9.
1472 81. Pellegrini, L.A.-O.X., Bonfio, C.A.-O., Chadwick, J., Begum, F., Skehel, M.A.-O., and
1473 Lancaster, M.A.-O. (2020). Human CNS barrier-forming organoids with cerebrospinal fluid
1474 production. LID - eaaz5626 [pii] LID - 10.1126/science.aaz5626 [doi].
1475 82. Pellegrini, L., and Lancaster, M.A. (2021). Breaking the barrier: In vitro models to study
1476 choroid plexus development. Curr Opin Cell Biol *73*, 41–49. 10.1016/j.ceb.2021.05.005.
1477 83. Schwerk, C., and Schroten, H. (2024). In vitro models of the choroid plexus and the blood-
1478 cerebrospinal fluid barrier: advances, applications, and perspectives. Hum Cell *37*, 1235–
1479 1242. 10.1007/s13577-024-01115-5.
1480 84. Montalban, X., Lebrun-Frenay, C., Oh, J., Arrambide, G., Moccia, M., Pia Amato, M.,
1481 Amezcua, L., Banwell, B., Bar-Or, A., Barkhof, F., et al. (2025). Diagnosis of multiple
1482 sclerosis: 2024 revisions of the McDonald criteria. Lancet Neurol *24*, 850–865.
1483 10.1016/S1474-4422(25)00270-4.
1484 85. Thompson, A.J., Banwell, B.L., Barkhof, F., Carroll, W.M., Coetzee, T., Comi, G.,
1485 Correale, J., Fazekas, F., Filippi, M., Freedman, M.S., et al. (2018). Diagnosis of multiple
1486 sclerosis: 2017 revisions of the McDonald criteria. Lancet Neurol *17*, 162–173.
1487 10.1016/S1474-4422(17)30470-2.
1488 86. Kurtzke, J.F. (1983). Rating neurologic impairment in multiple sclerosis: an expanded
1489 disability status scale (EDSS). Neurology *33*, 1444–1452. 10.1212/wnl.33.11.1444.

1490 87. Sipe, J.C., Knobler, R.L., Braheny, S.L., Rice, G.P., Panitch, H.S., and Oldstone, M.B.
1491 (1984). A neurologic rating scale (NRS) for use in multiple sclerosis. Neurology *34*, 1368–
1492 1372. 10.1212/wnl.34.10.1368.
1493 88. Strober, L., DeLuca, J., Benedict, R.H., Jacobs, A., Cohen, J.A., Chiaravalloti, N., Hudson,
1494 L.D., Rudick, R.A., LaRocca, N.G., and Multiple Sclerosis Outcome Assessments, C.
1495 (2019). Symbol Digit Modalities Test: A valid clinical trial endpoint for measuring cognition
1496 in multiple sclerosis. Mult Scler *25*, 1781–1790. 10.1177/1352458518808204.
1497 89. Rosti, E., Hamalainen, P., Koivisto, K., and Hokkanen, L. (2006). The PASAT performance
1498 among patients with multiple sclerosis: analyses of responding patterns using different
1499 scoring methods. Mult Scler *12*, 586–593. 10.1177/1352458506070624.
1500 90. Fame, R.M., Kalugin, P.N., Petrova, B., Xu, H., Soden, P.A., Shipley, F.B., Dani, N., Grant,
1501 B., Pragana, A., Head, J.P., et al. (2023). Defining diurnal fluctuations in mouse choroid
1502 plexus and CSF at high molecular, spatial, and temporal resolution. Nat Commun *14*,
1503 3720. 10.1038/s41467-023-39326-3.
1504 91. Slyper, M., Porter, C.B., Ashenberg, O., Waldman, J., Drokhlyansky, E., Wakiro, I., Smillie,
1505 C., Smith-Rosario, G., Wu, J., and Dionne, D. (2020). A single-cell and single-nucleus
1506 RNA-Seq toolbox for fresh and frozen human tumors. Nature medicine *26*, 792–802.
1507 92. Marsh, S.E., Walker, A.J., Kamath, T., Dissing-Olesen, L., Hammond, T.R., de Soysa,
1508 T.Y., Young, A.M.H., Murphy, S., Abdulraouf, A., Nadaf, N., et al. (2022). Dissection of
1509 artifactual and confounding glial signatures by single-cell sequencing of mouse and
1510 human brain. Nat Neurosci *25*, 306–316. 10.1038/s41593-022-01022-8.
1511 93. Young, M.D., and Behjati, S. (2020). SoupX removes ambient RNA contamination from
1512 droplet-based single-cell RNA sequencing data. GigaScience *9*.
1513 10.1093/gigascience/giaa151.
1514 94. Hao, Y., Stuart, T., Kowalski, M.H., Choudhary, S., Hoffman, P., Hartman, A., Srivastava,
1515 A., Molla, G., Madad, S., Fernandez-Granda, C., and Satija, R. (2023). Dictionary learning
1516 for integrative, multimodal and scalable single-cell analysis. Nature Biotechnology *42*,
1517 293–304. 10.1038/s41587-023-01767-y.
1518 95. McGinnis, C.S., Murrow, L.M., and Gartner, Z.J. (2019). DoubletFinder: Doublet Detection
1519 in Single-Cell RNA Sequencing Data Using Artificial Nearest Neighbors. Cell Systems *8*,
1520 329–337.e324. 10.1016/j.cels.2019.03.003.
1521 96. Fleming, S.J., Chaffin, M.D., Arduini, A., Akkad, A.-D., Banks, E., Marioni, J.C.,
1522 Philippakis, A.A., Ellinor, P.T., and Babadi, M. (2023). Unsupervised removal of systematic
1523 background noise from droplet-based single-cell experiments using CellBender. Nature
1524 Methods *20*, 1323–1335. 10.1038/s41592-023-01943-7.
1525 97. Hoffman, G.E., and Schadt, E.E. (2016). variancePartition: interpreting drivers of variation
1526 in complex gene expression studies. BMC Bioinformatics *17*. 10.1186/s12859-016-1323-
1527 z.
1528 98. Ritchie, M.E., Phipson, B., Wu, D., Hu, Y., Law, C.W., Shi, W., and Smyth, G.K. (2015).
1529 limma powers differential expression analyses for RNA-sequencing and microarray
1530 studies. Nucleic Acids Research *43*, e47–e47. 10.1093/nar/gkv007.
1531 99. Love, M.I., Huber, W., and Anders, S. (2014). Moderated estimation of fold change and
1532 dispersion for RNA-seq data with DESeq2. Genome Biology *15*. 10.1186/s13059-014-
1533 0550-8.
1534 100. Korotkevich, G., Sukhov, V., Budin, N., Shpak, B., Artyomov, M.N., and Sergushichev, A.
1535 (2021). Fast gene set enrichment analysis. bioRxiv, 060012. 10.1101/060012.
1536 101. Bharadwaj, R., Cimino, P.J., Flanagan, M.E., Latimer, C.S., Gonzalez-Cuyar, L.F., Juric-
1537 Sekhar, G., Montine, T.J., Marshall, D.A., and Keene, C.D. (2018). Application of the
1538 condensed protocol for the NIA-AA guidelines for the neuropathological assessment of
1539 Alzheimer's disease in an academic clinical practice. Histopathology *72*, 433–440.
1540 10.1111/his.13345.

102. Latimer, C.S., Burke, B.T., Liachko, N.F., Currey, H.N., Kilgore, M.D., Gibbons, L.E., Henriksen, J., Darvas, M., Domoto-Reilly, K., Jayadev, S., et al. (2019). Resistance and resilience to Alzheimer's disease pathology are associated with reduced cortical pTau and absence of limbic-predominant age-related TDP-43 encephalopathy in a community-based cohort. Acta Neuropathol Commun *7*, 91. 10.1186/s40478-019-0743-1.
103. Slyper, M., Porter, C.B.M., Ashenberg, O., Waldman, J., Drokhlyansky, E., Wakiro, I., Smillie, C., Smith-Rosario, G., Wu, J., Dionne, D., et al. (2020). A single-cell and single-nucleus RNA-Seq toolbox for fresh and frozen human tumors. Nat Med *26*, 792–802. 10.1038/s41591-020-0844-1.
104. Savola, S., Kaivola, K., Raunio, A., Kero, M., Makela, M., Parn, K., Palta, P., Tanskanen, M., Tuimala, J., Polvikoski, T., et al. (2022). Primary age-related tauopathy in a Finnish population-based study of the oldest old (Vantaa 85+). Neuropathol Appl Neurobiol *48*, e12788. 10.1111/nan.12788.
105. Alcolado, J.C., Moore, I.E., and Weller, R.O. (1986). Calcification in the human choroid plexus, meningiomas and pineal gland. Neuropathol Appl Neurobiol *12*, 235–250. 10.1111/j.1365-2990.1986.tb00137.x.
106. van Wetering, J., Geut, H., Bol, J.J., Galis, Y., Timmermans, E., Twisk, J.W.R., Hepp, D.H., Morella, M.L., Pihlstrom, L., Lemstra, A.W., et al. (2024). Neuroinflammation is associated with Alzheimer's disease co-pathology in dementia with Lewy bodies. Acta Neuropathol Commun *12*, 73. 10.1186/s40478-024-01786-z.
107. Shahidehpour, R.K., Nelson, P.T., Katsumata, Y., and Bachstetter, A.D. (2025). Exploring the link between dystrophic microglia and the spread of Alzheimer's neuropathology. Brain *148*, 89–101. 10.1093/brain/awae258.
108. Langkammer, C., Bredies, K., Poser, B.A., Barth, M., Reishofer, G., Fan, A.P., Bilgic, B., Fazekas, F., Mainero, C., and Ropele, S. (2015). Fast quantitative susceptibility mapping using 3D EPI and total generalized variation. Neuroimage *111*, 622–630. 10.1016/j.neuroimage.2015.02.041.
109. Cox, R.W. (1996). AFNI: software for analysis and visualization of functional magnetic resonance neuroimages. Comput Biomed Res *29*, 162–173. 10.1006/cbmr.1996.0014.
110. Fedorov, A., Beichel, R., Kalpathy-Cramer, J., Finet, J., Fillion-Robin, J.C., Pujol, S., Bauer, C., Jennings, D., Fennessy, F., Sonka, M., et al. (2012). 3D Slicer as an image computing platform for the Quantitative Imaging Network. Magn Reson Imaging *30*, 1323–1341. 10.1016/j.mri.2012.05.001.
111. Donnay, C., Dieckhaus, H., Tsagkas, C., Gaitan, M.I., Beck, E.S., Mullins, A., Reich, D.S., and Nair, G. (2023). Pseudo-Label Assisted nnU-Net enables automatic segmentation of 7T MRI from a single acquisition. Front Neuroimaging *2*, 1252261. 10.3389/fnimg.2023.1252261.
112. Wolf, F.A., Angerer, P., and Theis, F.J. (2018). SCANPY: large-scale single-cell gene expression data analysis. Genome Biology *19*. 10.1186/s13059-017-1382-0.
113. Lopez, R., Regier, J., Cole, M.B., Jordan, M.I., and Yosef, N. (2018). Deep generative modeling for single-cell transcriptomics. Nature Methods *15*, 1053–1058. 10.1038/s41592-018-0229-2.
114. Pan, S., Hu, R., Long, G., Jiang, J., Yao, L., and Zhang, C. (2018). Adversarially regularized graph autoencoder for graph embedding. arXiv preprint arXiv:1802.04407.
115. Fey, M., Sunil, J., Nitta, A., Puri, R., Shah, M., Stojanovi{{c}}, B. {., Bendias, R., Barghi, A., Kocijan, V., Zhang, Z., He, X., Lenssen, J. E., & Leskovec, J. (2025). PyG 2.0: Scalable Learning on Real World Graphs. Temporal Graph Learning Workshop @ KDD.
116. Wang, C., and Blei, D.M. (2018). A General Method for Robust Bayesian Modeling. Bayesian Analysis *13*. 10.1214/17-ba1090.

1590 117. Schindelin, J., Arganda-Carreras, I., Frise, E., Kaynig, V., Longair, M., Pietzsch, T.,
1591 Preibisch, S., Rueden, C., Saalfeld, S., Schmid, B., et al. (2012). Fiji: an open-source
1592 platform for biological-image analysis. Nat Methods *9*, 676–682. 10.1038/nmeth.2019.
1593 118. Phipson, B., Sim, C.B., Porrello, E.R., Hewitt, A.W., Powell, J., Oshlack, A., and Mathelier,
1594 A. (2022). propeller:testing for differences in cell type proportions in single cell data.
1595 Bioinformatics *38*, 4720–4726. 10.1093/bioinformatics/btac582.
1596 119. Aibar, S., González-Blas, C.B., Moerman, T., Huynh-Thu, V.A., Imrichova, H.,
1597 Hulselmans, G., Rambow, F., Marine, J.-C., Geurts, P., Aerts, J., et al. (2017). SCENIC:
1598 single-cell regulatory network inference and clustering. Nature Methods *14*, 1083–1086.
1599 10.1038/nmeth.4463.
1600 120. Gu, Z., Eils, R., and Schlesner, M. (2016). Complex heatmaps reveal patterns and
1601 correlations in multidimensional genomic data. Bioinformatics *32*, 2847–2849.
1602 10.1093/bioinformatics/btw313.
1603 121. Gu, Z., Gu, L., Eils, R., Schlesner, M., and Brors, B. (2014). circlizeimplements and
1604 enhances circular visualization in R. Bioinformatics *30*, 2811–2812.
1605 10.1093/bioinformatics/btu393.
1606 122. Waskom, M. (2021). seaborn: statistical data visualization. Journal of Open Source
1607 Software *6*. 10.21105/joss.03021.

1608

1609 **FIGURES AND FIGURE LEGENDS**

Figure 1

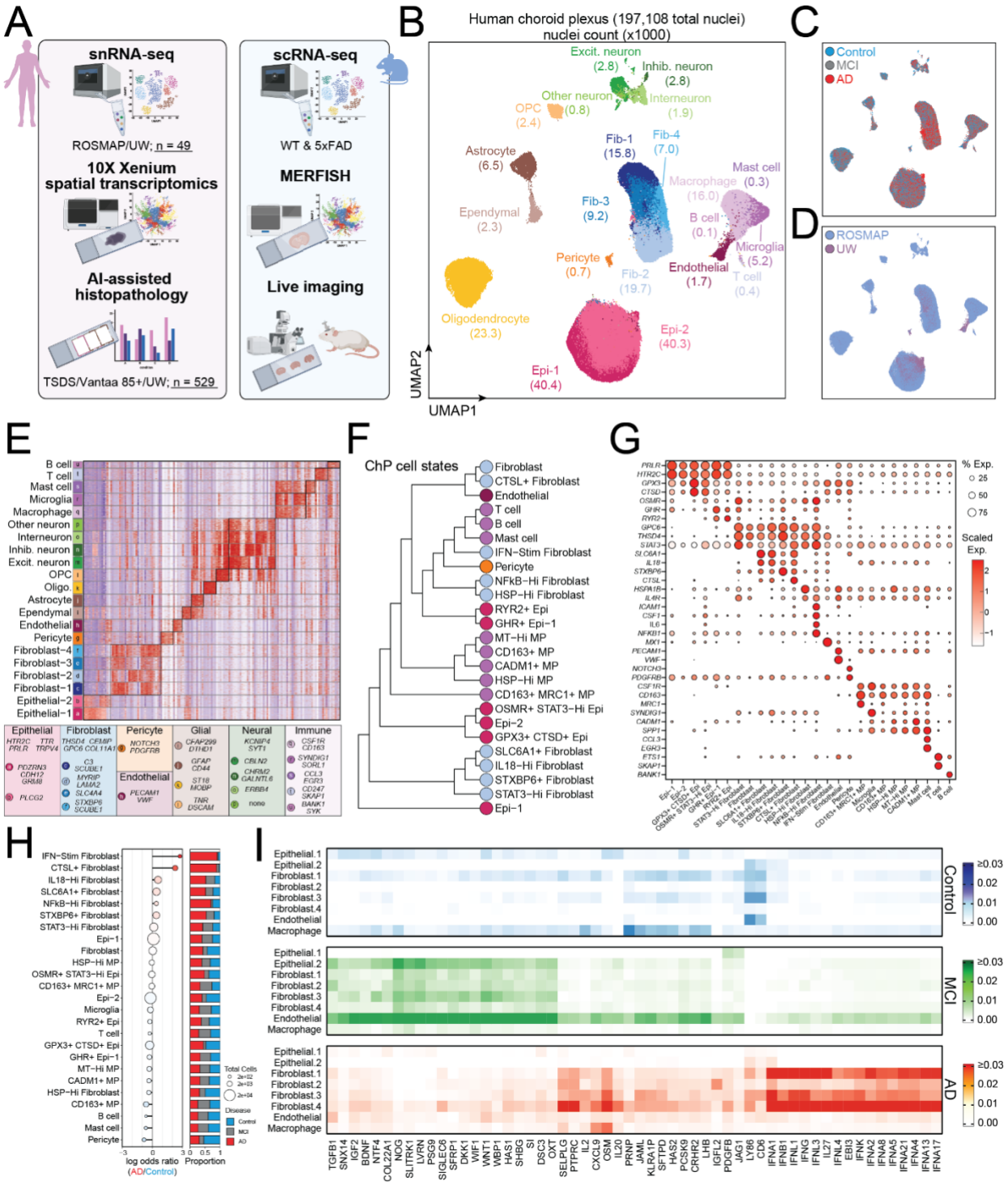

1610

1611 **Figure 1. A cellular atlas of the choroid plexus in AD reveals widespread inflammatory**
1612 **states.**
1613 (**A**) Schematic overview of the multi-modal study design. Human ChP was profiled using
1614 snRNA-seq, 10X Xenium spatial transcriptomics, and AI-assisted histopathology
1615 (TSDS/Vanta85+/UW, n=529 donors). Mouse ChP was profiled using scRNA-seq, MERFISH
1616 spatial transcriptomics, and *in vivo* two-photon imaging in WT and 5xFAD mice.
1617 (**B**) Uniform Manifold Approximation and Projection (UMAP) embeddings of 197,108 nuclei (49
1618 donors) isolated from human ChP colored by cell type annotations. Numbers indicate cell
1619 counts (x1000) per cell type.
1620 (**C**) UMAP colored by disease classification (Control: blue, mild cognitive impairment (MCI):
1621 grey, AD: red).
1622 (**D**) UMAP colored by study of origin (ROSMAP: blue, n=168,171, 31 donors; UW: purple,
1623 n=28,937, 18 donors).
1624 (**E**) Heatmap of marker gene expression across cell subtypes. Color scale represents gene
1625 expression as a z-score (navy: low, white: intermediate, red: high). Bottom panel: key marker
1626 genes organized by cell class.
1627 (**F**) Hierarchical clustering dendrogram of ChP cell states based on transcriptomic similarity.
1628 Clustering was performed using Ward's method on Euclidean distances of scaled average
1629 expression of variable genes. MP: macrophage; Epi: epithelial cells.
1630 (**G**) Dot plot of marker gene expression across cell states.
1631 (**H**) Compositional analysis of cell state abundance in AD versus Control. Left: Proportional
1632 regression analysis showing log odds ratio with Benjamini-Hochberg FDR values of enrichment
1633 of a cell state in AD (red) compared to Control (blue). Right: stacked bar plots showing disease
1634 group proportions for each cell state.
1635 (**I**) Heatmaps of predicted MultiNicheNet ligand activities across disease conditions. Only
1636 ligands predicted to activate target genes are shown.

Figure 2

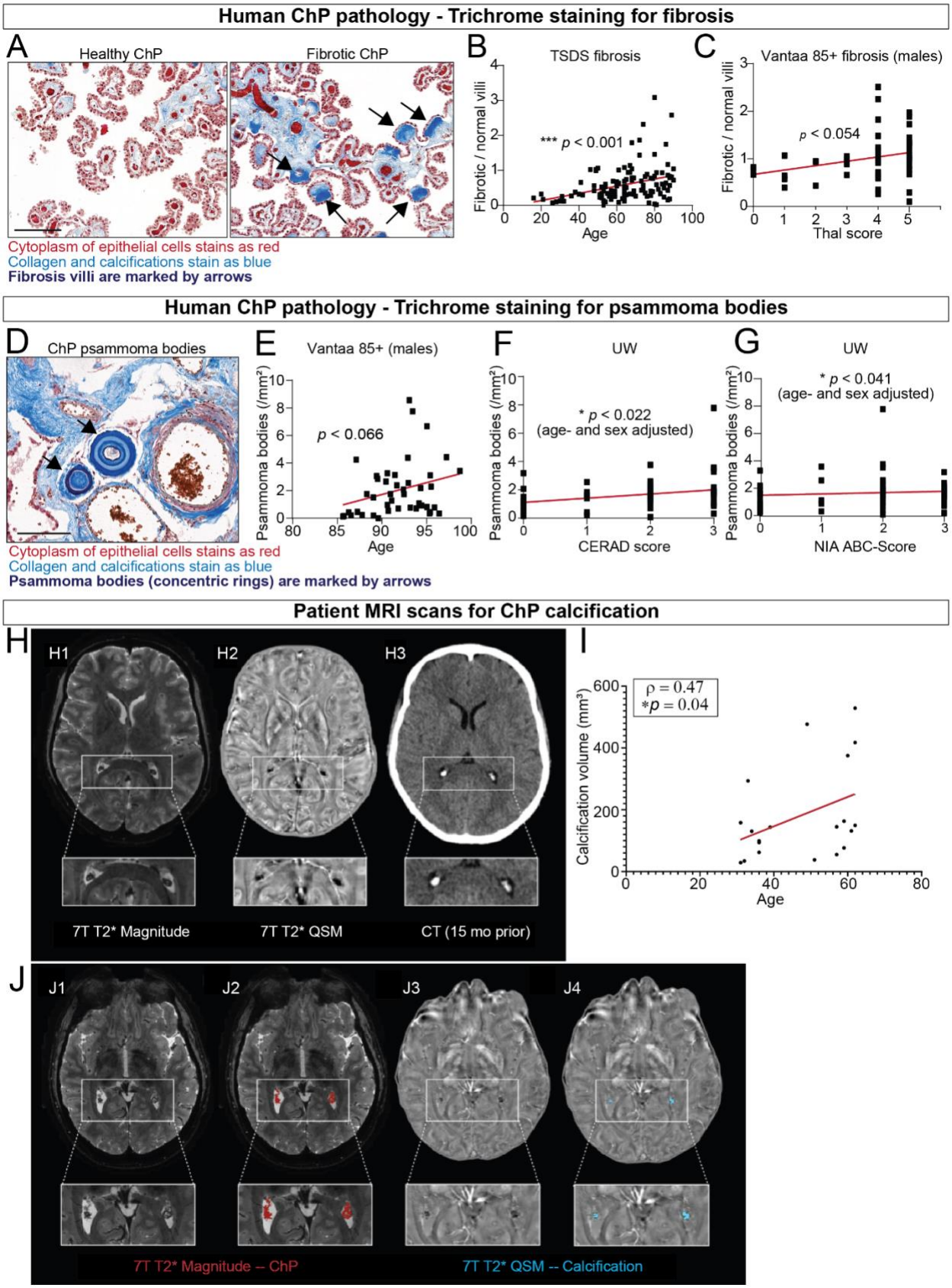

1637

1638 **Figure 2. AI-assisted histopathology identifies fibrosis and calcification as age-driven**
1639 **ChP pathologies in human**

1640 (**A**) Representative images showing trichrome stained human ChP sections from aged subjects.
1641 Condensed dark blue staining indicates fibrosis (marked by arrows). Scale = 300 μm.
1642 (**B**) Quantification by Aiforia showing the ratio of fibrotic versus healthy villi is associated with
1643 age in TSDS cohort (trichrome staining, simple linear regression model; $p < 0.001$).
1644 (**C**) Ratio of fibrotic per normal villi (quantified by Aiforia) in relation to Thal β-amyloid phases in
1645 males of the Vantaa 85+ cohort (trichrome staining, simple linear regression model; $p < 0.054$)
1646 (**D**) Representative images showing trichrome stained human ChP sections from aged subjects.
1647 Blue/reddish concentric lamellar/roundish structures indicate calcification (marked by arrows), in
1648 perivascular location. Scale = 300 μm.
1649 (**E**) Psammoma bodies (/mm^2) quantified by Aiforia on trichrome stainings in relation to age in
1650 males (Vantaa 85+, simple linear regression, $p < 0.066$).
1651 (**F, G**) Aiforia quantified Psammoma bodies (/mm^2) in the UW cohort are associated with
1652 CERAD (F; $p < 0.022$) and NIA-ABC (G; $p < 0.041$) scores (trichrome staining, linear regression
1653 adjusted for age and sex).
1654 (**H**) Representative images of patient MRI and CT scans. (D1) Choroid plexus from a 34-year-
1655 old woman with MS visualized with 7T T2* GRE. (D2) 7T T2* QSM demonstrated hypointense
1656 regions that are calcified, aligning with CT findings showing hyperdense calcified regions (D3).
1657 (**I**) Quantification of patient MRI scans showing calcification of the ChP is associated with age.
1658 (**J**) Representative images showing the segmentation of the ChP and calcification. (J1) Choroid
1659 plexus and the corresponding segmentation (J2) on 7T T2* GRE from a 31-year-old man with
1660 MS. (J3) Calcified hypointense regions on 7T T2* QSM were identified, and corresponding
1661 segmentations (J4) were created.
1662

Figure 3

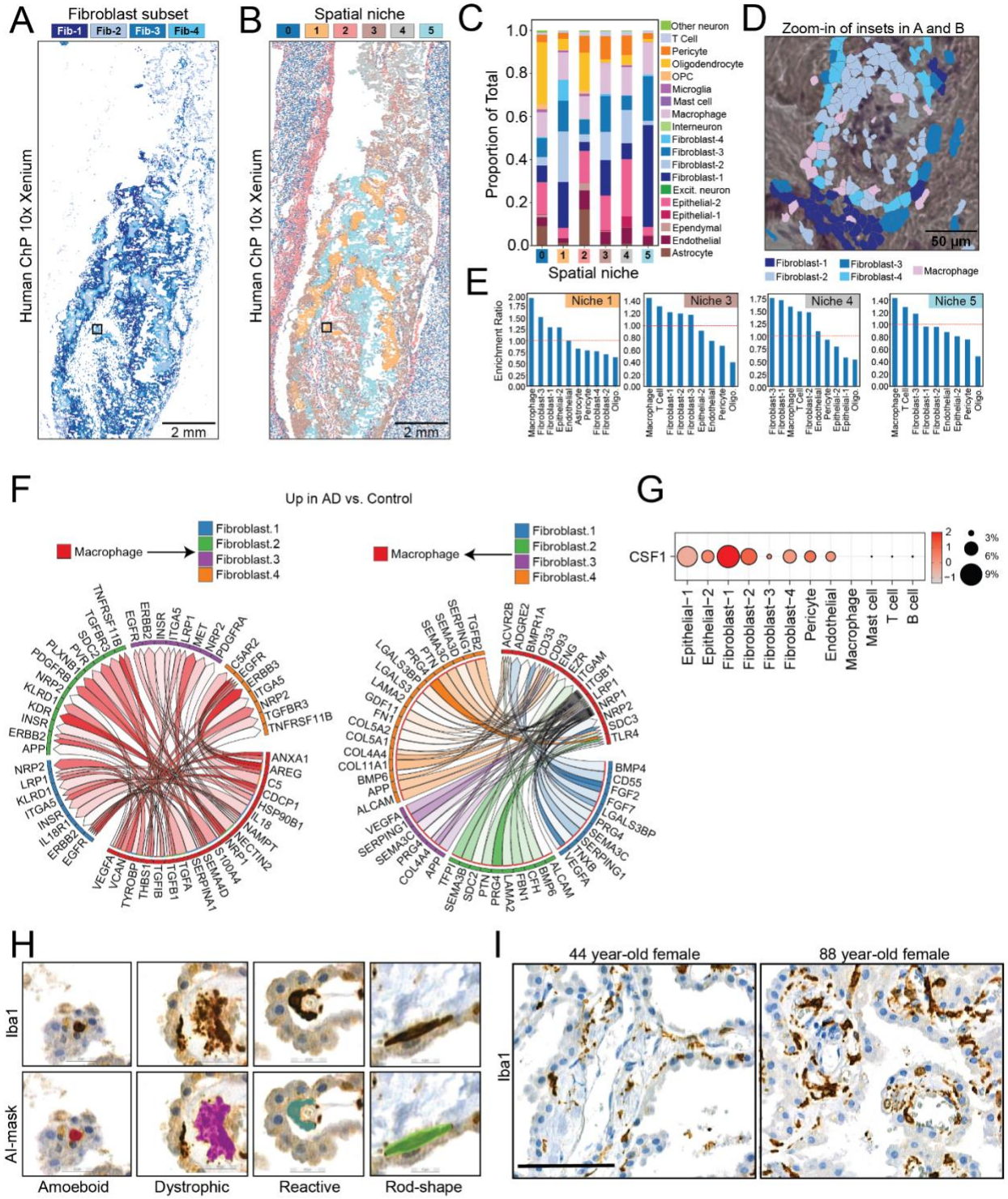
A
Fibroblast subset
Fib-1
Fib-2
Fib-3
Fib-4
Human ChP 10x Xenium
2 mm
B
Spatial niche
0
1
2
3
4
5
Human ChP 10x Xenium
2 mm
C
Proportion of Total
Spatial niche
Other neuron
T Cell
Pericyte
Oligodendrocyte
OPC
Microglia
Mast cell
Macrophage
Interneuron
Fibroblast-4
Fibroblast-3
Fibroblast-2
Fibroblast-1
Excit. neuron
Epithelial-2
Epithelial-1
Ependymal
Endothelial
Astrocyte
D
Zoom-in of insets in A and B
50 µm
Fibroblast-1
Fibroblast-3
Macrophage
Fibroblast-2
Fibroblast-4
E
Enrichment Ratio
Niche 1
Niche 3
Niche 4
Niche 5
F
Up in AD vs. Control
Macrophage
Fibroblast.1
Fibroblast.2
Fibroblast.3
Fibroblast.4
G
CSF1
Epithelial−1
Epithelial−2
Fibroblast−1
Fibroblast−2
Fibroblast−3
Fibroblast−4
Pericyte
Endothelial
Macrophage
Mast cell
T cell
B cell
3%
6%
9%
H
Iba1
AI-mask
Amoeboid
Dystrophic
Reactive
Rod-shape
I
44 year-old female
88 year-old female
Iba1

1664 **Figure 3. Spatial and single-nucleus transcriptomics identifies fibroblast-macrophage**
1665 **niches in human ChP**

1666 (**A**) Xenium cell type distributions reveal the differential localization of functionally varied choroid
1667 plexus fibroblast subtypes identified by snRNA-seq.

1668 (**B-C**) Graph embedding defines choroid plexus niches defined by distinct spatial distributions,
1669 anatomical characteristics, and cell type proportions. Scale bar: 2 mm. Black box indicates
1670 region shown in (D).

1671 (**D**) Spatial co-localization of choroid plexus macrophages and various fibroblast subtypes within
1672 spatial niche 1. Scale bar: 50 μm.

1673 (**E**) Choroid plexus macrophages display niche and region-specific interactions with fibroblast
1674 subtypes, epithelial cells, and other immune cells based on the relative frequency of cell-cell
1675 proximity.

1676 (**F**) Chord diagram depicting top 50 ligand-receptor interactions upregulated in AD versus
1677 Control (log2FC > 0.50 and $p<0.05$) between macrophages and fibroblast subtypes.

1678 (**G**) Dot plot of *CSF1* expression across ChP cell types.

1679 (**H**) Representative images showing Iba1+ macrophages of various morphology and their masks
1680 generated by Aiforia for quantification.

1681 (**I**) Representative images showing increased Iba1+ macrophage coverage in the ChP in aged
1682 humans. Scale = 100.

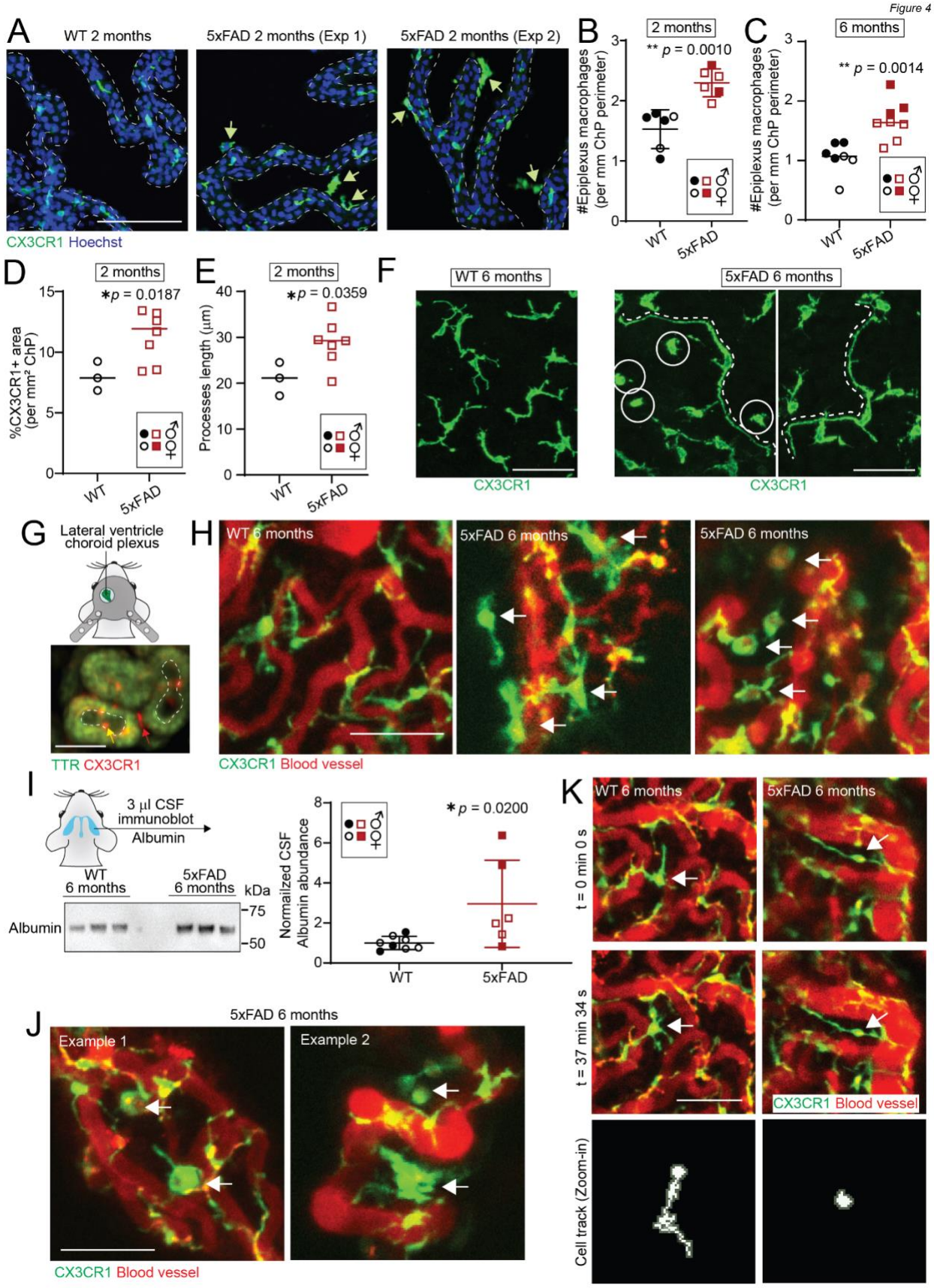
Figure 4
A
WT 2 months
5xFAD 2 months (Exp 1)
5xFAD 2 months (Exp 2)
CX3CR1 Hoechst
B
2 months
** p = 0.0010
#Epiplexus macrophages (per mm ChP perimeter)
WT
5xFAD
C
6 months
** p = 0.0014
D
2 months
*p = 0.0187
%CX3CR1+ area (per mm² ChP)
E
2 months
*p = 0.0359
Processes length (μm)
F
WT 6 months
5xFAD 6 months
CX3CR1
G
Lateral ventricle choroid plexus
TTR CX3CR1
H
WT 6 months
5xFAD 6 months
CX3CR1 Blood vessel
I
3 μl CSF immunoblot Albumin
WT 6 months
5xFAD 6 months
kDa
Albumin
75
50
Normalized CSF Albumin abundance
*p = 0.0200
J
5xFAD 6 months
Example 1
Example 2
CX3CR1 Blood vessel
K
WT 6 months
5xFAD 6 months
t = 0 min 0 s
t = 37 min 34 s
CX3CR1 Blood vessel
Cell track (Zoom-in)

1683

1684 **Figure 4. Mouse models of AD reveal abnormalities in macrophage behaviors**

1685 (**A**) Representative images showing increased number of epiplexus macrophages in the ChP of
1686 5xFAD mice as early as 2 months old. Scale = 100 µm.

1687 (**B-C**) Quantification showing the number of epiplexus macrophages per mm of ChP perimeter
1688 is higher in 5xFAD mice than WT controls at both 2 months (B, ** p = 0.0010) and 6 months old
1689 (C, ** p = 0.0014). Welch's t-test.

1690 (**D**) Quantification showing the total area of CX3CR1+ macrophages per mm^2 of ChP increases
1691 in 5xFAD mice at 2 months old. * p = 0.0187. Welch's t-test.

1692 (**E**) Quantification showing the average process length of CX3CR1+ ChP macrophages
1693 increases in 5xFAD mice at 2 months old. * p = 0.0359. Welch's t-test.

1694 (**F**) Representative images showing ChP macrophages with extremely long processes and no
1695 processes present in 5xFAD mice at 6 months. Scale = 50 µm.

1696 (**G**) Schematics and a representative image from a TTR^{mNeon}/$CX3CR1^{TdTomato}$ mouse showing *in*
1697 *vivo* visualization of the ChP through a cranial window and separation of epiplexus versus
1698 stromal macrophages. Epiplexus macrophages (red arrow) are seen on top of epithelial cells
1699 (Green, TTRmNeon+) with a clear distance to blood vessels (dotted outline), while stromal
1700 macrophages (yellow arrow) are immediately adjacent to blood vessels. Scale = 50 µm.

1701 (**H**) Representative snapshots of in vivo recordings showing WT ChP (left) versus two example
1702 FOVs of 5xFAD ChP that contain increased number of epiplexus macrophages (middle, white
1703 arrows) and ameboid epiplexus macrophages with red blood-borne dye (right, white arrows).
1704 Scale = 100 µm.

1705 (**I**) Representative blot and quantification showing increased CSF albumin levels in 6 months old
1706 5xFAD mice. * *p* = 0.0200. Mann-Whitney.

1707 (**J**) Representative snapshots of *in vivo* recordings showing two examples of macrophages with
1708 large vacuoles (white arrows) assembling phagocytic bubbles. Scale = 100 µm.

1709 (**K**) Representative snapshots of *in vivo* recordings at the beginning and the end showing lack of
1710 movement in the 5xFAD macrophage with extremely long processes. Scale = 100 μm. The
1711 tracks of the cell body of the chosen macrophages (white arrows) through the entire recordings
1712 are displayed at the bottom (with zoom-in for clarity).
1713 All quantitative data are presented as mean ± SD. Female mice are marked by unfilled legends.
1714

Figure 5

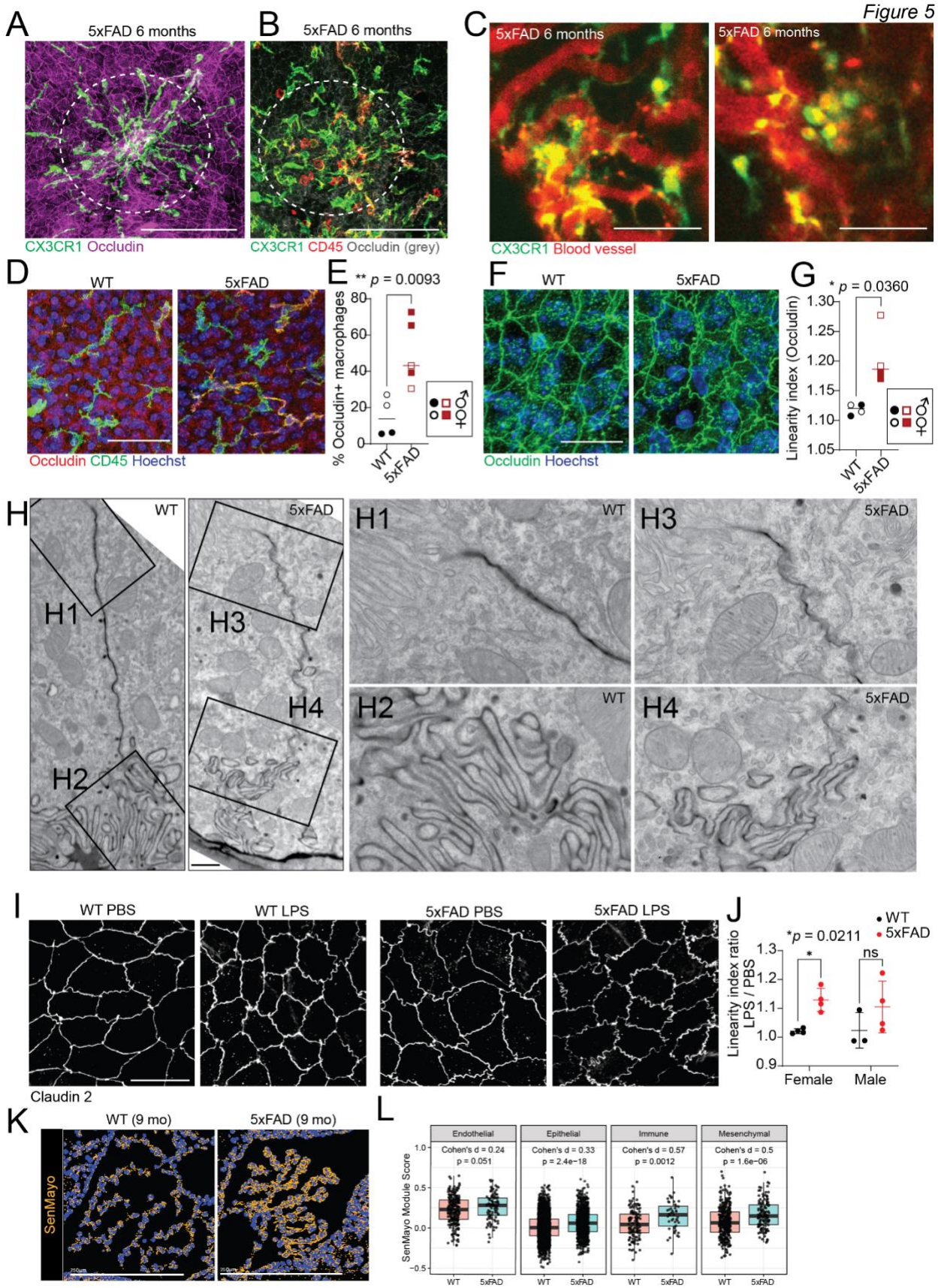

1715

1716 **Figure 5. Macrophages are involved in epithelial barrier dysregulation in mouse models**
1717 **of AD.**
1718 (**A-B**) Representative images showing clusters of CX3CR1+ macrophages and CD45-high
1719 peripheral immune cells at the ChP of 6 months old 5xFAD mice. Scale = 100 μm.
1720 (**C**) Representative snapshots of in vivo recordings showing two examples of macrophages
1721 clustering near blood vessels in the ChP of 6 months old 5xFAD mice. Scale = 100 μm.
1722 (**D-E**) Representative images and quantification showing increased portion of ChP
1723 macrophages stain positive for tight junction protein Occludin in 5xFAD mice at 6 months. Scale
1724 = 100 μm. ** p = 0.0093. Welch's t-test.
1725 (**F-G**) Representative images and quantification showing increased linearity index of epithelial
1726 cell-cell borders marked by tight junction protein Occludin, indicating barrier damage. Scale = 50
1727 μm. * p = 0.0360. Welch's t-test.
1728 (**H**) Representative images of electron microscopy of ChP epithelial cells showing "wavy" cell-
1729 cell borders in 6 months old 5xFAD mice. Cell-cell borders are labeled by retro-orbital infusion of
1730 HRP. H1 and H3 show the zoom-in views at the apical surface. H2 and H4 show the zoom-in
1731 views of the basal labyrinth. Scale = 1 μm.
1732 (**I-J**) Representative images and quantification showing delayed epithelial barrier recovery in
1733 female 5xFAD mice at 6 months old, shown by sustained high linearity index of cell-cell borders
1734 labeled by tight junction protein Claudin 2. Scale = 20 μm. * p = 0.0211. Welch's t-test.
1735 (**K-L**) Spatial transcriptomic analysis of 9 months 5xFAD mice ChP by MERFISH reveals that
1736 5xFAD mice ChP had increased senescence score (SenMayo) in major cell types including
1737 epithelial, immune, and mesenchymal cells.
1738 All quantitative data are presented as mean ± SD. Female mice are marked by unfilled legends.
1739
1740
1741

Figure 6

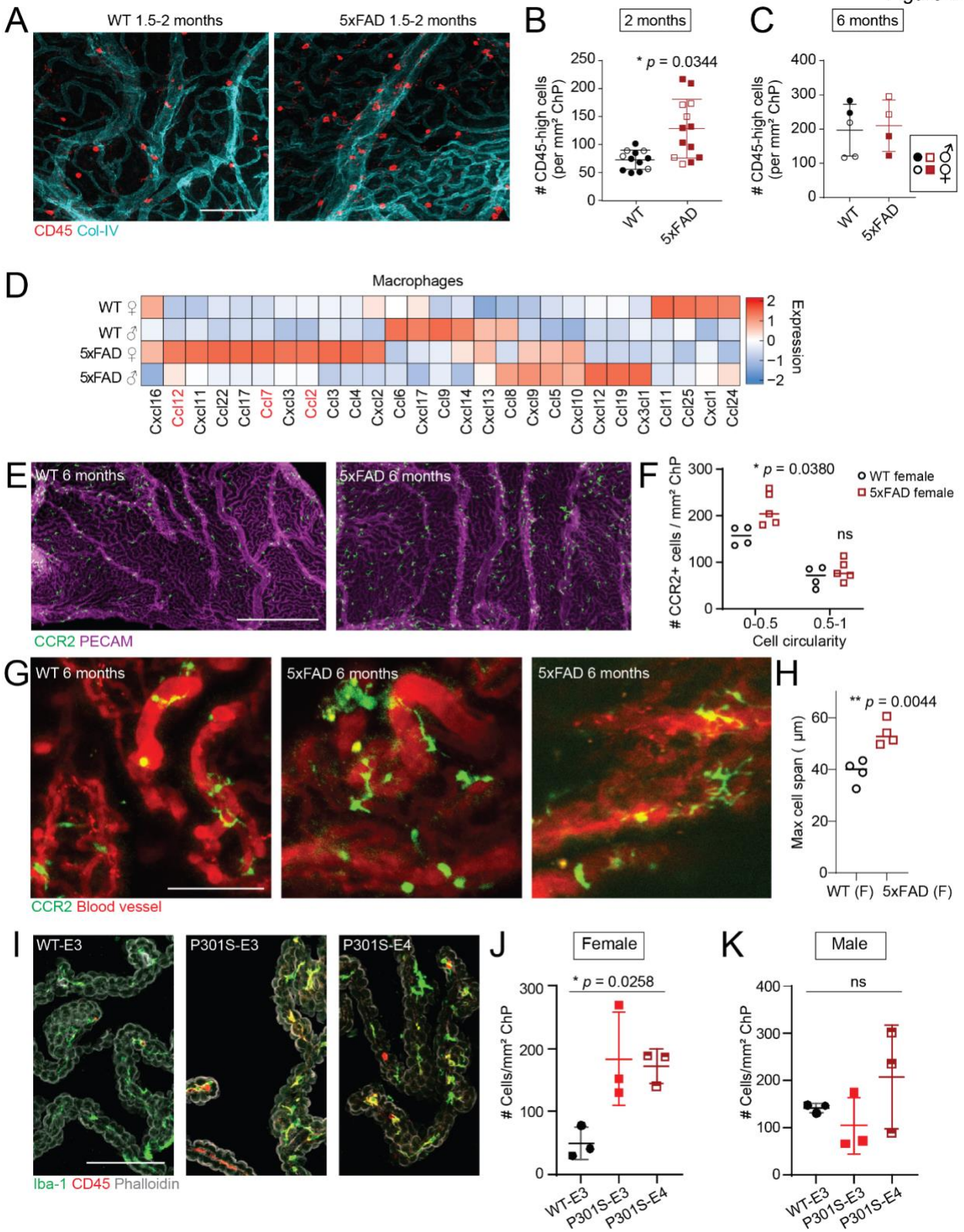

1742

1743 **Figure 6. Myeloid cells are recruited to the ChP in mouse AD models with sex**
1744 **dimorphism**

1745 (**A**) Representative images showing increased CD45-high peripheral immune cells in the ChP of
1746 5xFAD mice at 1.5-2 months old. Scale = 100 μm.

1747 (**B-C**) Quantifications showing increased CD45-high peripheral immune cells per mm^2 ChP in
1748 only 1.5-2 months and not 6 months old 5xFAD mice. * p = 0.0344 (2 months), Welch's t-test.

1749 (**D**) Gene expression of chemokines by sex and genotype from single-cell RNAseq of 5xFAD
1750 mice ChP at 6 months old; red = CCR2 ligand.

1751 (**E-F**) Representative images and quantifications showing female 5xFAD mice at 6 months old
1752 has increased number of CCR2+ cells with ramified macrophage-like morphology (low cell
1753 circularity). * p = 0.0380 (adjusted), Welch's t-test with multiple comparison correction by Holm-
1754 Sidak method.

1755 (**G**) Representative snapshots of in vivo recording showing two examples of 5xFAD females at 6
1756 months old having more macrophage-like CCR2+ cells. Scale = 100 μm.

1757 (**H**) Quantification of maximum span of individual CCR2+ cells from in vivo recordings showing
1758 female 5xFAD mice has increased cell span. ** *p* = 0.0044, Welch's t-test.

1759 (**I-K**) Representative images and quantifications showing 9 months old female P301S mice had
1760 increased CD45-high Iba1+ macrophages, regardless of APOE genotypes. * *p* = 0.0258,
1761 Welch's t-test.

1762 All quantitative data are presented as mean ± SD. Female mice are marked by unfilled legends
1763 unless separately marked.

1764 **SUPPLEMENTAL FIGURES AND FIGURE LEGENDS**

A

Study	Group	N	Sex ♂ : ♀	APOE ε2/ε3:ε2/ε4: ε3/ε3:ε3/ε4	Braak stage	Age at death (yrs)	NFT score	Amyloid score	C score	# of cells
ROSMAP	Control	9	4:5	0:0:4:5	2.89 ± 1.27	89.77 ± 6.16	0.18 ± 0.13	3.21 ± 3.82	2.33 ± 1.12	5519 ± 1409
	MCI	10	4:6	0:0:5:5	3.50 ± 1.08	86.47 ± 6.39	0.55 ± 0.64	4.39 ± 3.90	1.80 ± 0.42	5519 ± 2459
	AD	12	7:5	0:0:6:6	3.92 ± 1.88	89.40 ± 5.66	1.06 ± 1.26	4.39 ± 3.28	1.50 ± 0.52	5276 ± 3433
UW	Control	9	3:6	1:0:6:2	3.78 ± 1.20	89.67 ± 9.72	NA	NA	2.22 ± 1.30	1700 ± 1114
	AD	9	3:6	0:1:4:4	5.11 ± 0.93	89.22 ± 8.58	NA	NA	1.44 ± 0.53	1516 ± 988

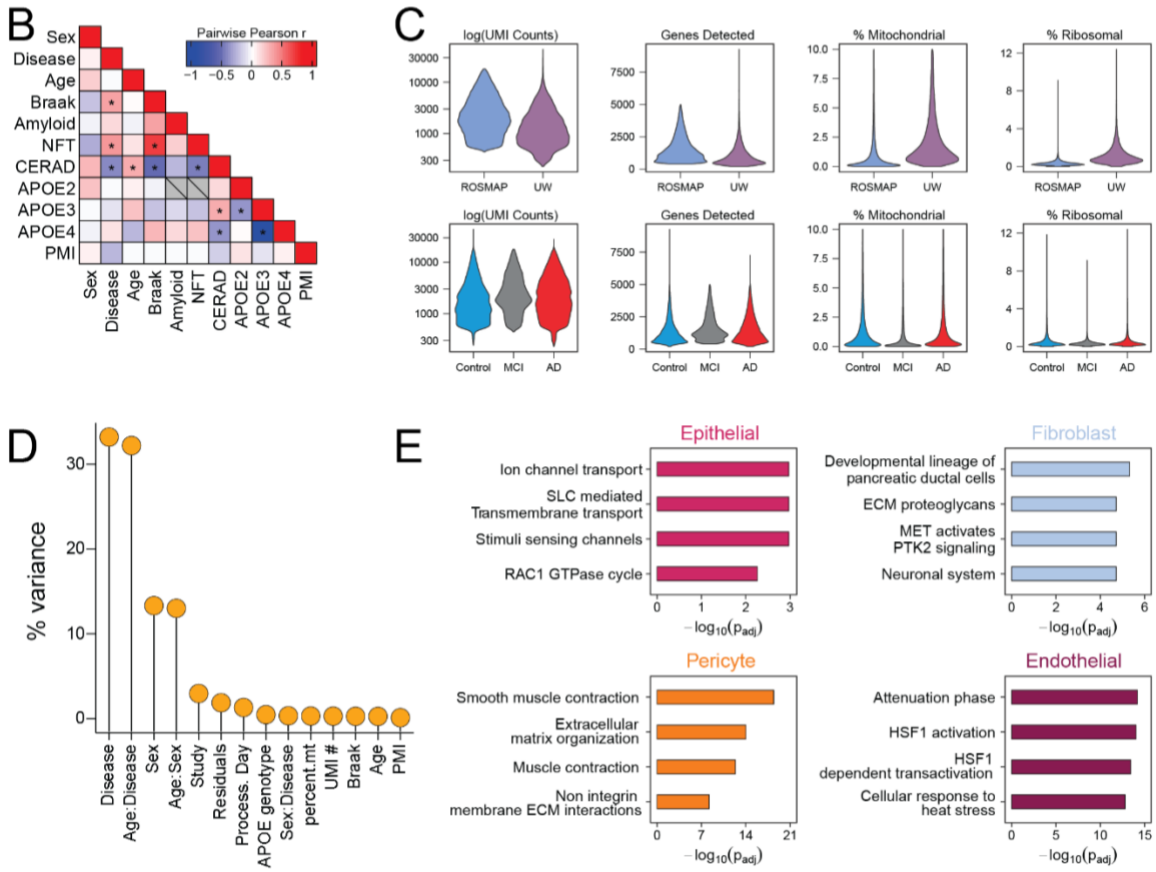

1765

1766 **Supplemental Figure 1. Cohort characteristics and quality control metrics for snRNA-seq,**

1767 **related to Figure 1.**

1768 (**A**) Summary table of donor demographics and pathological scores by study and disease group.

1769 (**B**) Pairwise Pearson correlation matrix of clinical and demographic variables. * = $p < 0.05$.

1770 NFT, neurofibrillary tangles; APOE2/3/4, number of respective APOE alleles; PMI, post-mortem

1771 interval.

1772 (**C**) Violin plot of snRNA-seq quality metrics by study (top) and disease status (bottom).

1773 (**D**) Percent variance in gene expression explained by technical and demographic covariates.

1774 (**E**) Gene set enrichment analysis for cell type marker genes.

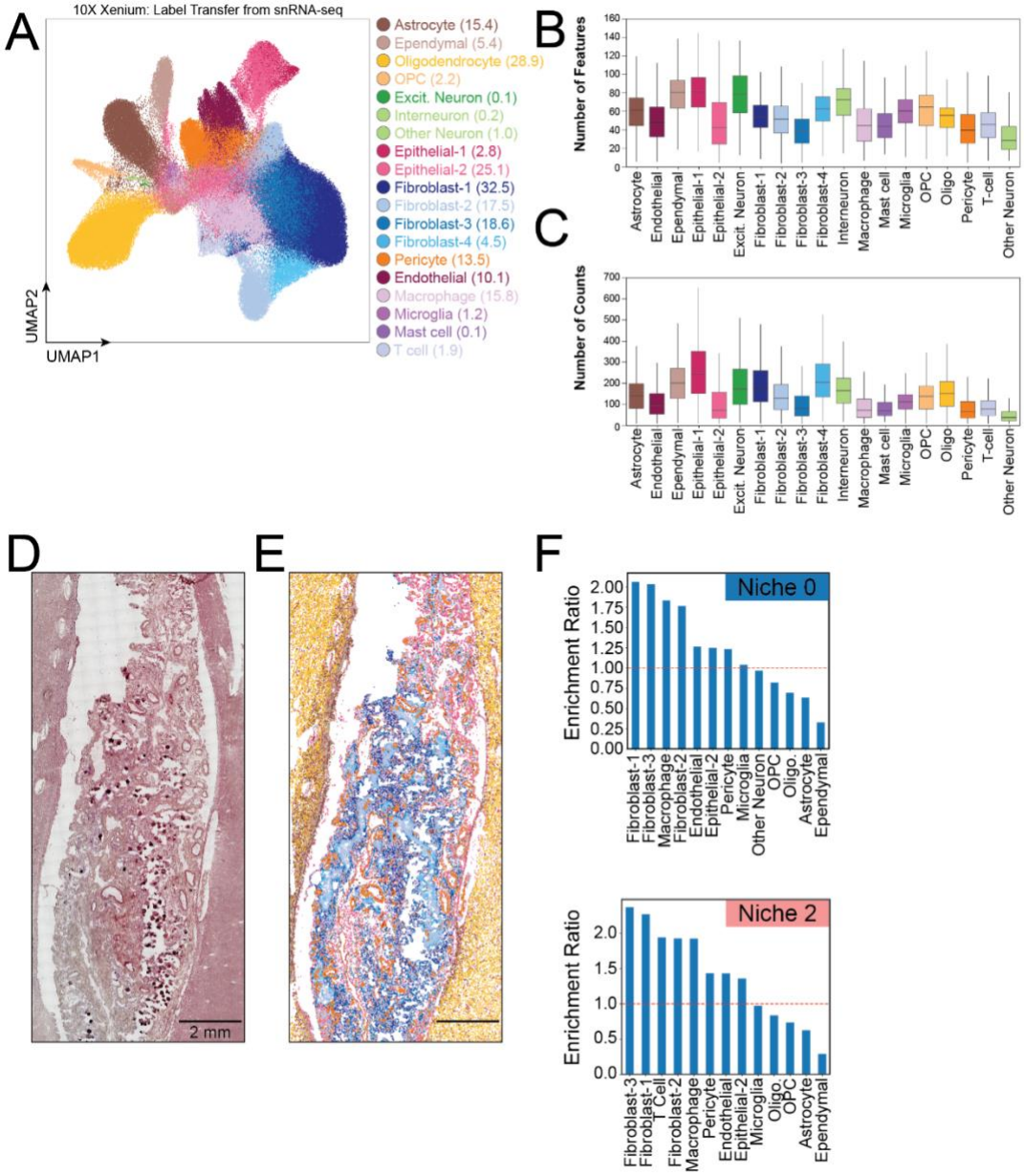

Supplemental Figure 2: Spatial transcriptomics quality control and niche characterization, related to Figure 3.

(**A**) UMAP visualization of Xenium data following label transfer from snRNA-seq reference. Cell type annotations and cell counts in legend.

(**B-C**) Box plots of QC metrics by cell type.

(**D**) H&E-stained section of human ChP tissue used for spatial transcriptomics.

1782 (**E**) Spatial map of the same tissue section colored by cell type assignment, colored by legend in

1783 (A).

1784 (**F**) Cell type enrichment ratio for spatial niches outside the ChP.

1785

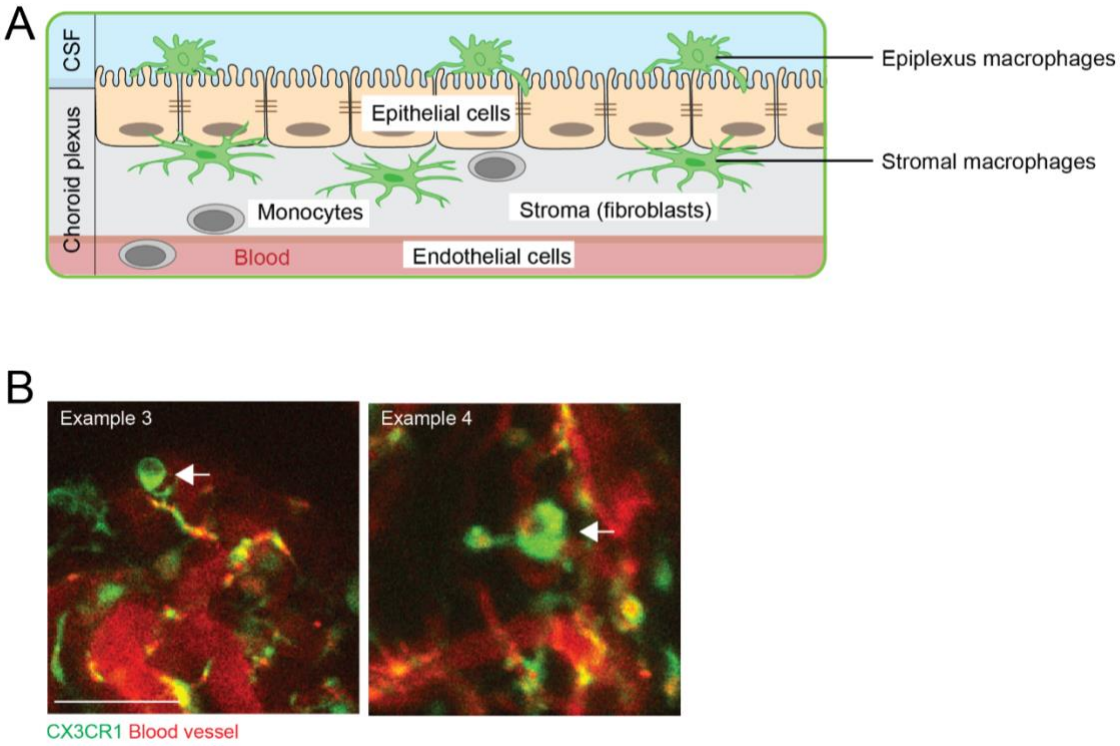

1786

1787 **Supplemental Figure 3. Related to Figure 4.**

1788 (**A**) Schematics showing the anatomy of the ChP, the connection of epithelial cells by tight

1789 junctions, and the positions of epiplexus and stromal macrophages.

1790 (**B**) Two additional examples showing macrophages with large vacuoles, as shown in Figure 4J.

1791 Scale = 100 μm

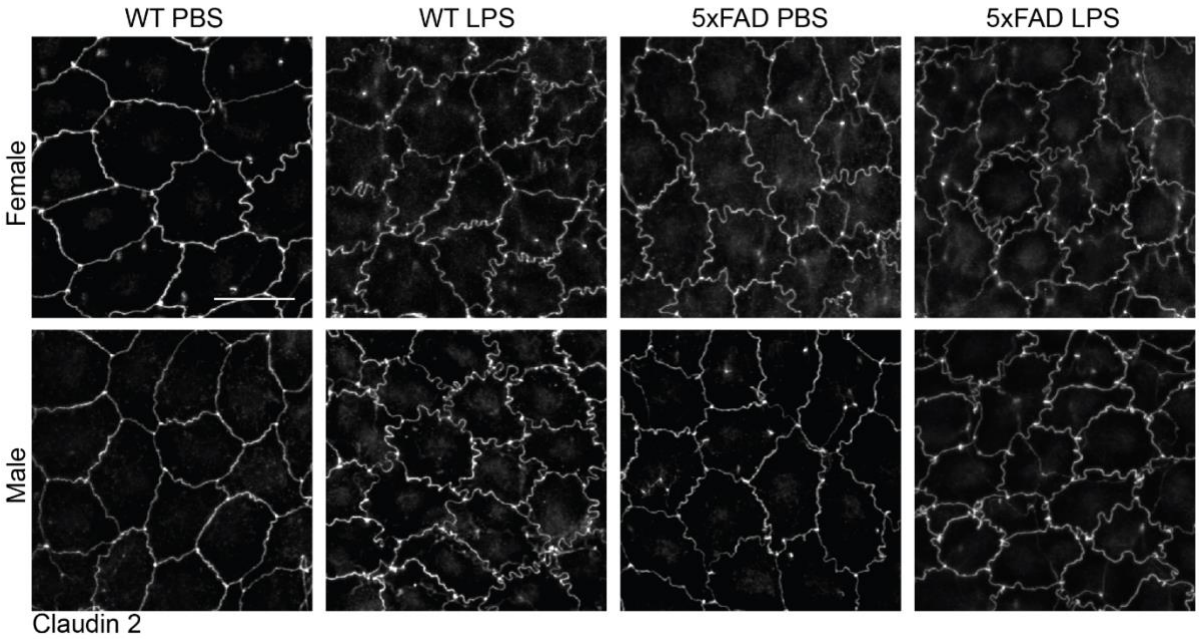

1792

1793 **Supplemental Figure 4. Related to Figure 5.** Disruption of epithelial tight junctions in both WT

1794 and 5xFAD mice by LPS at 24 hrs. Scale = 20 μm

1795

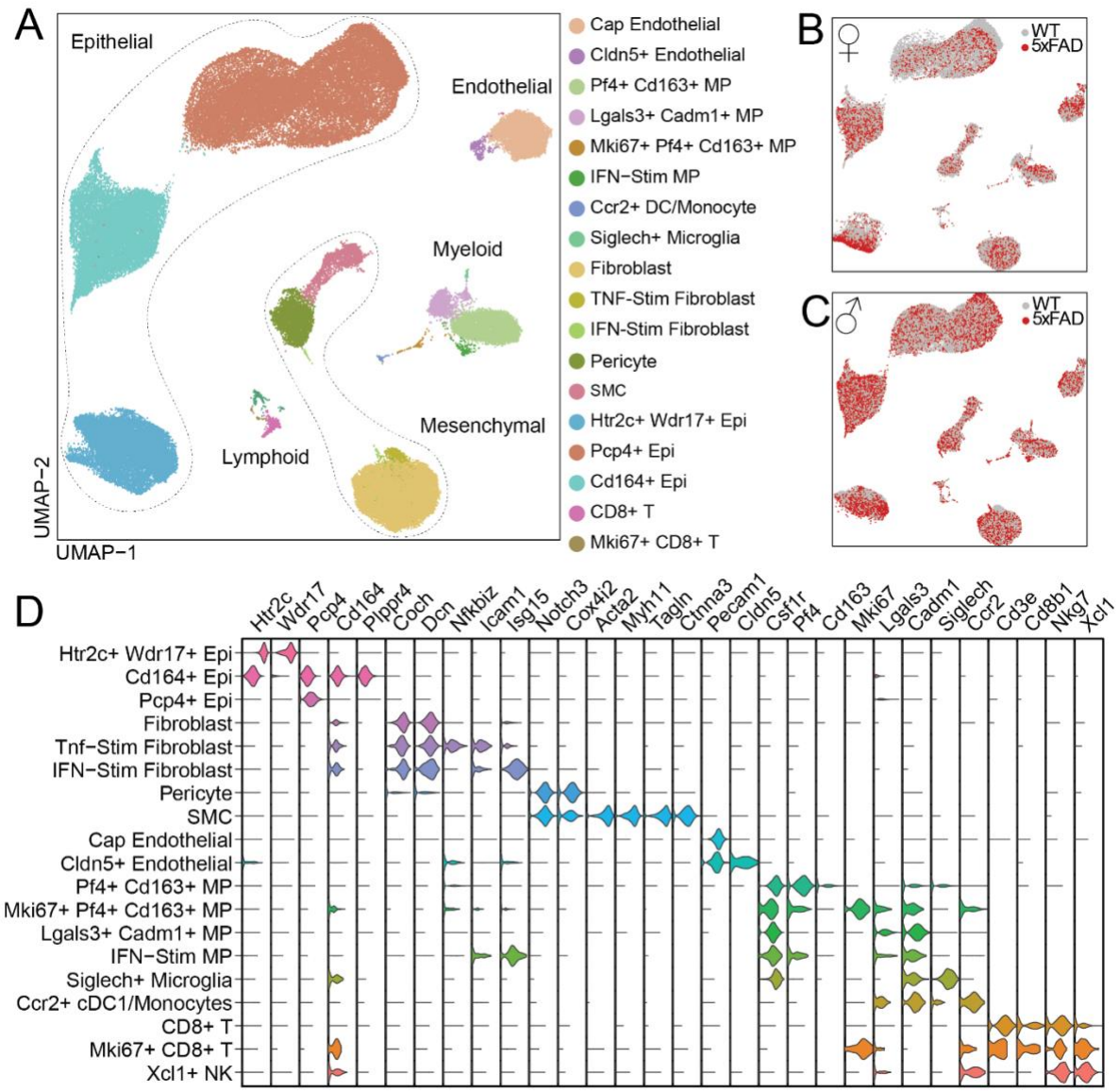

Supplemental Figure 5. Supporting data of single-cell RNAseq of 5xFAD mice ChP at 6 months, related to Figure 6.

(**A-C**) UMAP embeddings of cell states (A) and genotypes (B, females; C, males) in the 5xFAD mouse ChP at 6 months old.

(**D**) Violin plot of marker gene expression across ChP-resident cell states/end-clusters.

1804 **LIST OF SUPPLEMENTAL FILES**

1805 **Supplemental Data 1:** Patient metadata and cell type marker genes for human snRNA-seq

1806 **Supplemental Data 2:** Patient demographic information, methodology, and statistics of
1807 histopathology analyses

1808 **Supplemental Data 3:** Cell type marker genes for mouse ChP scRNA-seq

1809 **Supplemental Video 1:** 5xFAD mice ChP epiplexus macrophages had abnormal morphology
1810 and some contained blood-borne fluorescent dye. Green: CX3CR1+ macrophages. Red: 70kDa
1811 Dextran-TexasRed delivered I.P. to label blood vessels. Scale = 100 μm.

1812 **Supplemental Video 2:** 5xFAD mice ChP had epiplexus macrophages with long processes and
1813 reduced motility. Green: CX3CR1+ macrophages. Red: 70kDa Dextran-TexasRed delivered I.P.
1814 to label blood vessels. Scale = 100 μm.

1815 **Supplemental Video 3:** 5xFAD mice ChP had macrophages forming large clusters near blood
1816 vessels. Green: CX3CR1+ macrophages. Red: 70kDa Dextran-TexasRed delivered I.P. to label
1817 blood vessels. Scale = 100 μm.

1818 **Supplemental Video 4:** 5xFAD mice ChP had more CCR2+ cells with ramified macrophage-like
1819 morphology. Green: CCR2+ myeloid cells. Red: 70kDa Dextran-TexasRed delivered I.P. to label
1820 blood vessels. Scale = 100 μm.